Star formation and AGN feedback in the local Universe: Combining LOFAR and MaNGA[*]

C. R. Mulcahey[1,2] , S. K. Leslie[1,3] , T. M. Jackson[4,5,6], J. E. Young[2], I. Prandoni[7], M. J. Hardcastle[8], N. Roy[9], K. Małek[10,11], M. Magliocchetti[12], M. Bonato[7,13], H. J. A. Röttgering[1], and A. Drabent[14]

[1] Leiden Observatory, Leiden University, PO Box 9513, 2300 RA Leiden, The Netherlands
e-mail: leslie@strw.leidenuniv.nl
[2] Mount Holyoke College, Department of Astronomy, 50 College St, South Hadley, MA 01075, USA
e-mail: mulca23c@mtholyoke.edu
[3] ARC Centre of Excellence for All Sky Astrophysics in 3 Dimensions (ASTRO 3D), Australia
[4] Tuparev Astrotech, 3 Sofiyski Geroi Str, Sofia 1612, Bulgaria
[5] Astrosysteme Austria, Galgenau 19, 4212 Neumarkt im Mühlkreis, Austria
[6] Astronomisches Rechen-Institut, Zentrum für Astronomie der Universität Heidelberg, Mönchhofstr. 12-14, 69120 Heidelberg, Germany
[7] INAF – Istituto di Radioastronomia and Italian ALMA Regional Centre, Via Gobetti 101, 40129 Bologna, Italy
[8] Centre for Astrophysics Research, University of Hertfordshire, College Lane, Hatfield AL10 9AB, UK
[9] Department of Astronomy & Astrophysics, University of California, 1156 High Street, Santa Cruz, CA 95060, USA
[10] National Centre for Nuclear Research, ul. Hoża 69, 00-681 Warszawa, Poland
[11] Aix Marseille Univ. CNRS, CNES, LAM, Marseille, France
[12] INAF-IAPS, Via Fosso del Cavaliere 100, 00133 Roma, Italy
[13] INAF – Osservatorio Astronomico di Padova, Vicolo dell'Osservatorio 5, 35122 Padova, Italy
[14] Thüringer Landessternwarte (TLS), Sternwarte 5, 07778 Tautenburg, Germany

ABSTRACT

The effect of active galactic nuclei (AGN) on their host galaxies – in particular their levels of star formation – remains one of the key outstanding questions of galaxy evolution. Successful cosmological models of galaxy evolution require a fraction of energy released by an AGN to be redistributed into the interstellar medium to reproduce the observed stellar mass and luminosity function and to prevent the formation of over-massive galaxies. Observations have confirmed that the radio-AGN population is energetically capable of heating and redistributing gas at all phases, however, direct evidence of AGN enhancing or quenching star formation remains rare. With modern, deep radio surveys and large integral field spectroscopy (IFS) surveys, we can detect fainter synchrotron emission from AGN jets and accurately probe the star-forming properties of galaxies, respectively. In this paper, we combine data from the LOw Frequency ARray Two-meter Sky Survey (LoTSS) with data from one of the largest optical IFS surveys, Mapping Nearby Galaxies at Apache Point Observatory (MaNGA), to probe the star-forming properties of 307 local ($z < 0.15$) galaxies that host radio-detected AGN (RDAGN). We compare our results to a robust control sample of non-active galaxies that each match the stellar mass, redshift, visual morphology, and inclination of a RDAGN host. We find that RDAGN and control galaxies have broad star-formation rate (SFR) distributions, typically lie below the SFMS, and have negative stellar light-weighted age gradients. These results indicate that AGN selected based on their current activity are not responsible for suppressing their host galaxies' star formation. Rather, our results support the maintenance mode role that radio AGN are expected to have in the local Universe.

Key words. galaxies: active – galaxies: jets – galaxies: star formation – radio continuum: galaxies

1. Introduction

How supermassive black holes (SMBHs) and their host galaxies coevolve has yet to be fully understood. During growth periods, in which SMBHs actively accrete gas and are known as active galactic nuclei (AGN), they can release an enormous amount of radiation across the entire electromagnetic spectrum and can form winds and jets in their host galaxies. Current cosmological models of galaxy evolution (e.g., Bower et al. 2006; Schaye et al. 2015; Pillepich et al. 2019) require AGN to inject energy and momentum into their host galaxies' circum-ambient gas and interstellar medium (ISM) to reproduce the

observed stellar mass and luminosity function and prevent the formation of over-massive galaxies. Observationally, the relation between star-formation (SF) history and the growth of SMBHs at the center of galaxies has been the subject of many studies (e.g., Mullaney et al. 2012; Chen et al. 2013; Hickox et al. 2014, and references therein) that have found that SFRs and black hole accretion rates are intimately tied at all redshifts (e.g., Boyle & Terlevich 1998; Aird et al. 2015). This relationship likely indicates that SFRs and black hole accretion share a common fuel source (e.g., Silverman et al. 2009). The correlation between the mass of the black hole and the stellar velocity dispersion ($M_{BH}-\sigma_*$; e.g., Haehnelt & Kauffmann 2000) as well as the link between M_{BH} and the mass of the stellar bulge ($M_{BH}-M_{buldge}$; e.g., Häring & Rix 2004) further hint at the coevolution of black holes and stellar bulges, thereby suggesting

---

[*] Resolved ionization classification maps and $\sum$SFR maps for the full sample of 307 RDAGN galaxies and their assigned control galaxies are available upon request from the authors.

a link between black hole accretion rates and SFRs. However, studies investigating the relation between AGN activity and star-forming activity (e.g., Netzer 2009; Rosario et al. 2012; Gürkan et al. 2015; Stanley et al. 2015; Jackson et al. 2020) have so far yielded mixed results.

There are two prominent ways that AGN feedback can affect its host galaxy. Outflows from AGN can enhance SF (positive feedback) by compressing molecular clouds (e.g., Schaye et al. 2015) and/or the ISM (e.g., Ishibashi & Fabian 2012). Direct evidence of positive feedback is rare (e.g., Cresci et al. 2015; Shin et al. 2019; Nesvadba et al. 2020) and is typically observed in a companion satellite along the host galaxy's radio axis (e.g., Klamer et al. 2004; Croft et al. 2006; Feain et al. 2007; Rodríguez Zaurín et al. 2007; Elbaz et al. 2009; Crockett et al. 2012; Gilli et al. 2019). Conversely, AGN can suppress SF (negative feedback) via mechanical energy from winds, outflows, or jets heating the surrounding ISM and preventing molecular gas from radiatively cooling or due to AGN-driven outflows expelling gas from the host galaxy (e.g., Binney & Tabor 1995; Ciotti & Ostriker 2001, 2007; Croton et al. 2006; McNamara & Nulsen 2007; Nesvadba et al. 2008, 2010; Cattaneo et al. 2009; Ciotti et al. 2010; Fabian 2012; Yuan & Narayan 2014; Heckman & Best 2014). On longer timescales, jets can heat the circumgalactic and halo gas, preventing the cooling of gas and future SF (e.g., Ciotti & Ostriker 2001, 2007; McNamara & Nulsen 2007). Furthermore, the role of AGN feedback varies depending on the type of AGN the galaxy hosts. Radio-loud AGN can either be radiatively efficient or radiatively inefficient. Radiatively efficient AGN are typically connected to the most luminous AGN and accrete gas close to the Eddington limit from an optically thick, geometrically thin accretion disk. Radio-loud quasi-stellar objects and high excitation radio galaxies (HERGs) – further classifications of radiatively efficient AGN – are capable of producing powerful, two-sided jets that produce synchrotron radiation detectable at radio wavelengths. Energy released from the accretion disk may be capable of driving massive outflows of gas and may ultimately remove it from the potential well (e.g., Cattaneo et al. 2009; Fabian 2012). Conversely, radiatively inefficient AGN – also referred to as low excitation radio galaxies (LERGs) – are linked to low-to-intermediate-luminosity AGN and contain geometrically-thick, advection-dominated accretion flows, which can also produce powerful radio jets. Radiatively inefficient AGN have been shown to inject heat into their surroundings at a rate that is commensurate with the rate of cooling from the intergalactic medium, and are responsible for maintaining galaxy quiescence (e.g., Binney & Tabor 1995; Ciotti & Ostriker 2001, 2007; Bower et al. 2006; McNamara & Nulsen 2007; Cattaneo et al. 2009; Ciotti et al. 2010; Fabian 2012; Yuan & Narayan 2014; Heckman & Best 2014; Smolčić et al. 2017; Hardcastle et al. 2019).

Significant advances in our understanding of the effect of radio-mode AGN on their host galaxies have been achieved by coupling radio surveys such as the National Radio Astronomy Observatory (NRAO) Very Large Array Sky Survey (NVSS; 1.4 GHz continuum; Condon et al. 1998), the Faint Images of the Radio Sky at Twenty centimeters (FIRST; 1.4 GHz continuum; Becker et al. 1995), the Very Large Array Sky Survey (VLASS; 2−4 GHz; Hales 2013), and the Tata Institute of Fundamental Research (TIFR) Giant Metrewave Radio Telescope (GMRT) Sky Survey (TGSS; 150 MHz; Intema et al. 2017) with optical spectroscopic surveys such as the Sloan Digital Sky Survey (SDSS; York et al. 2000; Stoughton et al. 2002, and refer-

ences therein) and the Two-degree-Field Galaxy Redshift Survey (2dFGRS; Colless et al. 2001). Statistical studies that have combined these surveys (e.g., Best et al. 2005a,b; Sadler et al. 2002) have improved our understanding of the physical properties and prevalence of radio-AGN activity, but the nature of AGN emitting at radio frequencies lower than 1.4 GHz is yet to be fully understood. Sabater et al. (2019) combined data from the first data release (DR1) of the Low-Frequency Array (LOFAR; 10−240 MHz; van Haarlem et al. 2013) Two-Metre Sky Survey (LoTSS; Shimwell et al. 2017) with optical spectroscopic data from SDSS DR7 (Abazajian et al. 2009) and found that the most massive AGN host galaxies ($>10^{11}\,M_*$) always exhibit radio-AGN activity. These results suggest that radio-AGN activity is dictated by the host galaxy's fuel supply and that radio-AGN play a significant role in maintaining quiescence.

Simultaneously, integral field spectroscopy (IFS) surveys are revolutionizing our understanding of AGN by enabling more detailed investigations than previously possible. Unlike long-slit spectroscopy, which obtains a spectrum for a single point in the galaxy, or acquiring spectra along a "slice" of the galaxy, IFS obtains resolved, two-dimensional spectra across the surface of the galaxy. Integral field spectroscopy, in combination with stellar population modeling, permits the spatially resolved study of a galaxy's properties, such as current SFRs, metallicities, and stellar ages. Moreover, the gas and stellar kinematics over an entire galaxy can be obtained, enabling the effect of winds and dynamical disturbances to be examined. One of the largest optical IFS surveys is the Mapping Nearby Galaxies at Apache Point Observatory (MaNGA; Bundy et al. 2015) survey, which is one of three core parts of the fourth phase of SDSS (SDSS-IV). MaNGA has acquired observations with a spatial resolution of 2″.5 for ∼10 000 unique, low-redshift ($0.01 < z < 0.15$; median $z = 0.03$), massive ($M_* > 10^9\,M_\odot$) galaxies (Yan et al. 2016a). Previous MaNGA AGN studies underscore the importance of spatially resolved measurements to provide unprecedented insight into the prevalence and properties of AGN and their host galaxies (e.g., Rembold et al. 2017; Sánchez et al. 2018; Wylezalek et al. 2018, 2020; Comerford et al. 2020). Moreover, multiple IFS studies (e.g., Sánchez et al. 2018; Comerford et al. 2020; Wylezalek et al. 2020; Venturi et al. 2021) have found evidence for AGN driving outflows and turbulence and suppressing SF over time.

In this study, we build and improve on these previous works by coupling IFS data from MaNGA DR16 (Bundy et al. 2015; Ahumada et al. 2020) with data from the second data release of LoTSS (Shimwell et al. 2022). By leveraging the unique capabilities of LOFAR, our sample contains fainter radio-AGN – as well as remnant emission from sources that have recently shut off their jet activity – than those that have been previously analyzed with MaNGA data. We will determine where in relation to the SFMS the AGN host galaxies and non-active galaxies lie, compare the distribution of SFRs in regions ionized by hot stars, and will investigate how the age of stellar populations in AGN galaxies and non-active galaxies change as a function of galactocentric radius. We describe the sample and data used to achieve our research goals in Sect. 2. After outlining the methods used to define the radio-detected AGN (RDAGN) and control sample in Sect. 3, we determine these galaxies' relation to the star-forming main sequence (SFMS) in Sect. 4. In Sects. 5 and 6, we examine the spatially resolved properties of the stellar and nebular gas populations and probe their stellar light-weighted age gradients, respectively. Finally, we discuss our interpretation of these results and present a summary of our

conclusions in Sects. 7 and 8. Throughout this work, we assume the cosmological parameters of $H_0 = 70 \, \text{km} \, \text{s}^{-1}$, $\Omega_M = 0.3$ and a Salpeter initial mass function (IMF; Salpeter 1955).

2. Sample and data

This work makes use of the second data release of LoTSS, which is an ongoing radio continuum (120−168 MHz) survey of the northern sky. The scientific objectives of LoTSS are to exploit the unique capabilities of LOFAR to shed new light on the formation and evolution of massive black holes, cluster galaxies, and the high-redshift Universe (see Shimwell et al. 2019, and references therein). LoTSS uses LOFAR's high band antennas (HBA) and aims to reach a sensitivity <0.1 mJy beam^{-1} at an angular resolution of ~6″. LoTSS DR2 (Shimwell et al., in prep.) covers 27% of the northern sky and is composed of two discrete fields – denoted the 0 h and 13 h fields – covering 5700 deg^2 in total (1480 deg^2 in the 0 h field and 4240 deg^2 in the 13 h field). The astrometric accuracy of the images is ~0.2″. The flux calibration of LOFAR DR2 is uncertain to <10%.

MaNGA uses the Baryon Oscillation Spectroscopic Survey (BOSS) spectrograph (Smee et al. 2013) on the 2.5-m telescope at Apache Point Observatory (APO; Gunn et al. 2006) to obtain high-resolution ($R \sim 2000$) spectra over a large wavelength range (3600−10 300 Å). MaNGA uses integral field units (IFUs) that consist of tightly packed hexagonally bundled 2″ fibers, which have five different sizes (19, 37, 61, 91 and 127 fibers) corresponding to physical diameters of 12″, 17″, 22″, 27″, and 32″ (Drory et al. 2015). Raw fiber spectra have a calibration accuracy better than 5% (Yan et al. 2016a,b). We use MaNGA observations from the sixteenth data release of SDSS-IV, which includes observations of 4824 galaxies taken before August 2018 (Ahumada et al. 2020). Final data cubes and row stacked spectra (RSS) were produced using the MaNGA DRP (Law et al. 2016). Global emission line fluxes used in this study were obtained from the Portsmouth Group (Thomas et al. 2013). In addition, we use measured galaxy properties from several MaNGA Value Added Catalogs (VACs). We relied on the Pipe3D VAC (Sánchez et al. 2016a,b, 2018) for cumulative stellar mass (M_*) measurements, SFR (obtained from stellar population modeling), and stellar, light-weighted age gradient (α; slope of the gradient of the luminosity-weighted log-age of the stellar population within a galactocentric distance of 0.5 to $2.0 R_e$). To determine the morphological classifications of galaxies, we use T-TYPE values from the Morphology Deep Learning DR15 Value Added Catalog (VAC; Domínguez Sánchez et al. 2018). We probe the environment in which these galaxies reside using measurements from the Galaxy Environment for MaNGA (GEMA) VAC (Argudo-Fernández et al. 2015, and in prep.). Finally, D_n4000 and M_* values used in the D_n4000 versus $L_{1.4\,\text{GHz}}/M_*$ diagram (see Sect. 3.1) were taken from the MPA-JHU VAC[1].

Wide-Field Infrared Survey Explorer (WISE; Wright et al. 2010) data used in this work come from unWISE forced photometry performed by Lang et al. (2016) on un-blurred co-added WISE images (Lang 2014) at over 400 million optical SDSS source positions. Therefore, the unWISE data are naturally connected to the SDSS parent sample from which MaNGA targets were drawn.

The sky position of the LoTSS and MaNGA catalogs were matched using Tool for OPerations on Catalogues And Tables (TOPCAT). We matched the two source catalogs using a 5″

matching radius in RA and Dec. We estimate the total fraction of spurious matches to be <10% based on the average of 15 simulated MaNGA catalogs with randomized positions. Based on the cross-matching criteria, there are 1410 sources detected between the LoTSS and MaNGA survey. We use the SDSS spectroscopic ID (specObjID) to cross match the MaNGA-LoTSS catalog with the MPA-JHU catalog and with the global emission line flux catalog. For the Pipe3D, Morphology Deep Learning, and GEMA value added catalogs, we used the MANGAID identifier for cross matching.

3. Sample selection and properties

3.1. Selecting radio-detected AGN

The most reliable method for building a sample of pure radio-AGN is to select objects whose radio luminosity greatly surpasses that from their SF (Hardcastle et al. 2016, 2019; Calistro Rivera et al. 2017; Smolčić et al. 2017). In this work, we chose to separate our AGN host galaxies from SF galaxies using global optical emission-line properties, radio luminosities, and mid-infrared luminosities following the approach used by Sabater et al. (2019). We chose to take a multiwavelength approach in order to build a complete AGN sample with varying host galaxy properties. However, we highlight a subsample of classical radio-loud AGN (RLAGN), which is composed of RDAGN whose radio emission is higher than what is expected from their SFR alone based on our third diagnostic technique.

The first technique is the D_n4000 versus $L_{1.4\,\text{GHz}}/M_*$ diagram, which was developed by Best et al. (2005a), and it is shown in the upper upper left panel of Fig. 1. This method uses the strength of the 4000 Å break (D_n4000) in each galaxy's spectrum as a function of the ratio of the radio luminosity to stellar mass. This diagnostic diagram was developed using 1.4 GHz data, so we converted the LoTSS radio luminosity from 150 MHz to 1.4 GHz by assuming the established spectral index value of $\alpha = 0.7$ ($S_\nu \propto \nu^{-\alpha}$; Condon et al. 2002; Smolčić et al. 2017). We use D_n4000 and M_* values from the MPA-JHU VAC. Best et al. (2005a) demonstrated that because D_n4000 and $L_{1.4\,\text{GHz}}/M_*$ both depend on the SFR of galaxies, SF galaxies will populate a similar region in the D_n4000 versus $L_{1.4\,\text{GHz}}/M_*$ plane. Moreover, SF galaxies can be separated from AGN host galaxies because they will typically have a weaker D_n4000 values than AGN host galaxies of a comparable radio luminosity. The curved division line between SF/radio-quiet AGN and radio-AGN represents the 3 Gyr exponential SF track (Best et al. 2005a)[2]. At $D_n4000 > 1.7$ we replace the 3 Gyr exponential SF track with a horizontal line, as proposed by Sabater et al. (2019). The purpose of the addition is to avoid misclassifying AGN galaxies with large D_n4000 values as SF galaxies. The second diagnostic line is defined by $D_n4000 = 1.45 − 0.55 \times (L_{1.4\,\text{GHz}}/M_* − 12.2)$ (Best & Heckman 2012). All sources that lie above the 3 Gyr exponential SF track and to the right of this second line are classified as radio-AGN. Conversely, galaxies that fall above the 3 Gyr exponential SF track and to the left of the second diagnostic line are intermediate, which means that both SF and AGN activity likely contribute to the radio emission. Finally, all sources that lie below the 3 Gyr exponential SF track are classified as SF/radio-quiet AGN.

The second technique that we use to separate AGN galaxies from SF galaxies is [NII] Baldwin, Phillips & Telervich (BPT; Baldwin et al. 1981) diagram, which is shown in the upper right

---

[1] VAC created by the Max Planck for Astrophysics (MPA) and Johns Hopkins University (JHU) groups.

[2] The tracks used in this study were provided by Philip Best.
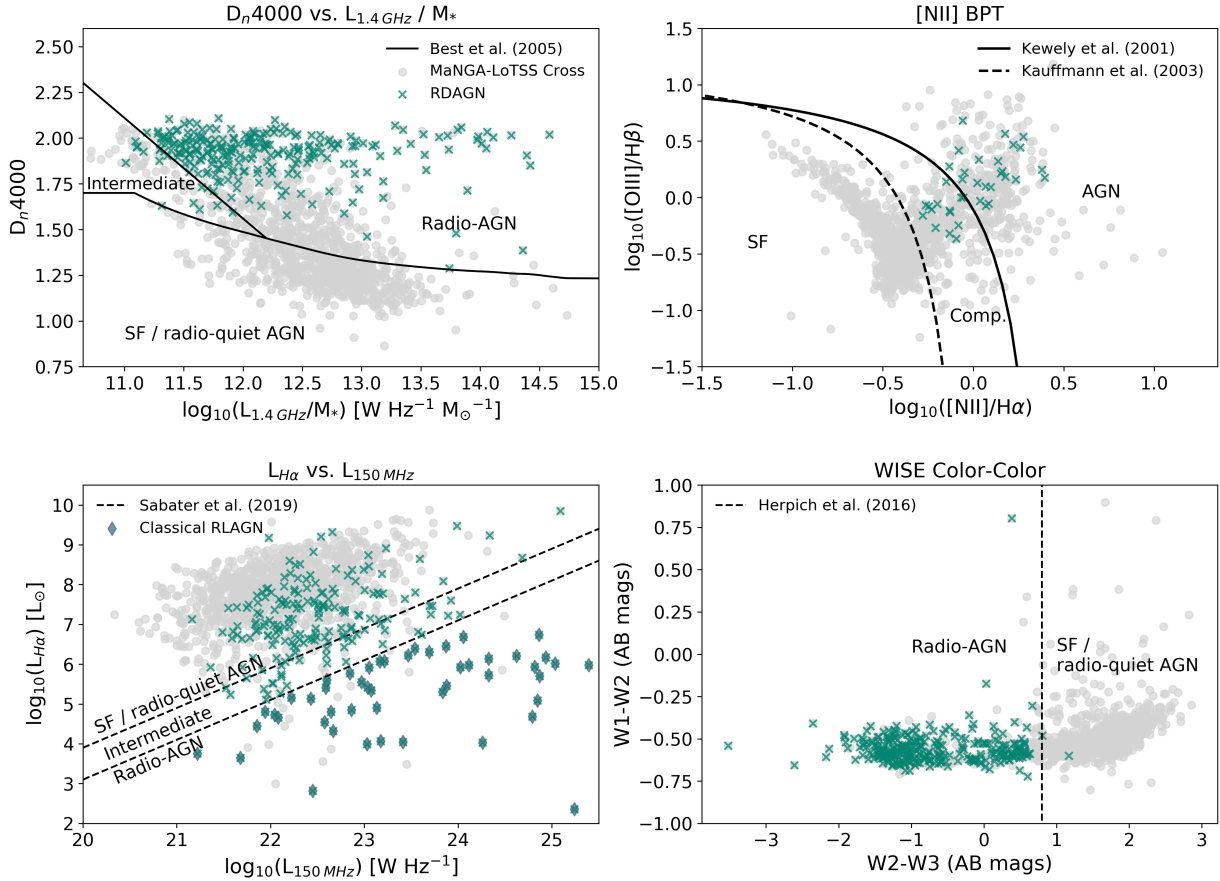
Fig. 1. Location of the RDAGN host galaxies on the four diagnostic diagrams used to separate galaxies whose radio emission was from SF from those galaxies likely powered by AGN. *Top row from left to right*: D_n4000 versus $L_{1.4\,\text{GHz}}/M_*$ from Best et al. (2005b), the [NII]/Hα BPT diagram (Baldwin et al. 1981). *Bottom row from left to right*: $L_{\text{H}\alpha}$ versus $L_{150\,\text{MHz}}$, WISE $W1-W2$ versus $W2-W3$ color-color diagram. The lines in each diagram represent division between SF/radio-quiet AGN, intermediate, and radio AGN. The final RDAGN sample, obtained following our criteria described in Sect. 2, is indicated by green "x's". The gray circles represent the full sample of MaNGA-LoTSS galaxies. Classical RLAGN are represented on the $L_{\text{H}\alpha}$ versus $L_{150\,\text{MHz}}$ diagram with dark gray diamonds.

panel of Fig. 1. For this diagnostic, we use global emission line fluxes that were obtained by the Portsmouth Group (Thomas et al. 2013). The diagram utilizes the ratio of narrow lines [OIII] $\lambda5007$ to Hβ and [NII] $\lambda6583$ to Hα to separate SF galaxies, from composite galaxies (a mix of ionizing sources likely contribute to the emission), from AGN galaxies. These line ratios can separate SF galaxies from AGN galaxies because the emission lines are affected by the hardness of the ionizing radiation field and the ionizing parameter. AGN galaxies will therefore have enhanced [NII]/Hα ratios because they have a harder ionizing radiation field than SF galaxies. The first diagnostic line on this diagram, represented by the solid, black line in Fig. 1, is the maximum starburst line from Kewley et al. (2001), which is defined by (log([OIII]/Hβ) < $0.61/(\log([\text{NII}]/\text{H}\alpha)-0.47)+1.19$). Unlike Sabater et al. (2019), we include the "composite" classification on the [NII] BPT (classification "Int" in Table 1). This second diagnostic line, represented by the dashed, black line in Fig. 1 separates pure SF galaxies from composite galaxies (Kauffmann et al. 2003) and is defined by log([OIII]/Hβ) < $0.61/(\log([\text{NII}]/\text{H}\alpha) - 0.05) + 1.3$. Using the Kauffman line results in a more complete AGN-host selection than the Kewley classification, but it is far from a pure AGN selection as, for example, hot low-mass evolved stars, and shock ionization can also produce composite line ratios (e.g., Sánchez 2020). For our [NII] BPT classification, we also require

all galaxies to have EW(Hα) > 3 Å to avoid passive galaxies whose ionization is dominated by old stars (e.g., Stasińska et al. 2008).

A limitation of the global BPT diagrams is that average or integrated emission line ratios are affected by various galactic properties; galaxies are rarely only "star-forming", "AGN", or "quiescent". Extinction may bias this selection, but because emission-line ratios are close together in wavelength ([NII] and Hα) and ([OIII] and Hβ), we expect similar extinction values for each line and therefore do not expect extinction to significantly bias our results. The optical narrow-line ratios of Type 1 AGN will have lower [NII]/Hα values than Type 2 AGN because the AGN are unobscured and the narrow emission lines are "blended" with broad emission lines (e.g., Zhang et al. 2008; Stern & Laor 2013). There is only one Type 1 AGN in our final RDAGN sample (plateifu 8549−12702), which we identified using the SDSS-DR7 Type 1 AGN catalog developed by Oh et al. (2015). Emission line ratios can also be enhanced by other non-AGN activity, such as Wolf-Rayet stars (e.g., Brinchmann et al. 2008), post-asymptotic giant branch stars (e.g., Binette et al. 1994; Yan & Blanton 2012; Belfiore et al. 2016), and shocks driven by galaxy mergers, jets, and stellar winds (e.g., Rich et al. 2011; Kewley et al. 2013). We explore these other mechanisms in Sect. 5.1.

Our third technique, which is shown in the bottom left panel of Fig. 1, is the relation between the luminosity of Hα ($L_{\mathrm{H}\alpha}$) and the LoTSS radio luminosity ($L_{150\,\mathrm{MHz}}$). Using the global emission line fluxes measured by the Portsmouth Group (Thomas et al. 2013), we measured the dust-corrected $L_{\mathrm{H}\alpha}$ using the average, R_V-dependent extinction function from Cardelli et al. (1989) and assume R_V to be 3.1 (Savage & Mathis 1979; Cardelli et al. 1989). Direct measurements of a galaxy's SFR can be determined from $L_{\mathrm{H}\alpha}$ and, in the absence of an AGN, $L_{150\,\mathrm{MHz}}$. Therefore, the locus of SF galaxies on the $L_{\mathrm{H}\alpha}$ versus $L_{150\,\mathrm{MHz}}$ diagram is separate from the locus of AGN host galaxies. The diagnostic lines to separate SF galaxies from AGN galaxies are adopted from Sabater et al. (2019): $\log_{10}(L_{\mathrm{H}\alpha}/L_\odot) = \log_{10}(L_{150\,\mathrm{MHz}}/\mathrm{W\,Hz}^{-1}) - 16.9$ and $\log_{10}(L_{\mathrm{H}\alpha}/L_\odot) = \log_{10}(L_{150\,\mathrm{MHz}}/\mathrm{W\,Hz}^{-1}) - 16.1$. Galaxies that lie below the bottom diagnostic line are classified as radio-AGN, intermediate if the galaxies lie between the two lines, and SF/radio-quiet AGN if the galaxies lie above the top diagnostic line. Our classical RLAGN subsample (52 galaxies in total) consists of the RDAGN host galaxies classified as a radio-AGN on this diagram (represented by the gray diamonds).

Our final method of separating AGN host galaxies from SF galaxies is the $W1-W2$ versus $W2-W3$ mid-infrared WISE colors diagnostic diagram, which is shown in the lower right panel of Fig. 1. We obtain the mid-infrared WISE colors from the unWISE forced photometry catalog of 400 million SDSS sources Lang et al. (2016). WISE colors are useful for detecting both obscured and unobscured AGN because hot dust surrounding AGN radiates strongly in mid-infrared emission. Following Sabater et al. (2019), we use the division from Herpich et al. (2016) where galaxies with $W2-W3 < 0.8$ mag (AB) are radio-AGN.

We select our radio-detected AGN (RDAGN) sample by combining the classifications from these four selection techniques to determine an overall classification for each galaxy in the MaNGA-LoTSS catalog. In the diagnostic diagrams presented in Fig. 1, galaxies can be classified as radio-AGN, SF, intermediate, or unclassified (i.e., low signal-to-noise ratio (S/N) or no measurement), which results in 192 unique combinations of classifications. When choosing the final classification, we weighted each classification from the diagnostic diagrams equally. Galaxies classified as intermediate in the D_n4000 versus $L_{1.4\,\mathrm{GHz}}/M_*$, [NII] BPT diagrams, or $L_{\mathrm{H}\alpha}$ versus $L_{150\,\mathrm{MHz}}$ were chosen to "favor" AGN over SF in order to build the most complete sample of AGN possible. For example, if a galaxy's classification is intermediate in the D_n4000 versus $L_{150\,\mathrm{MHz}}/M_*$ and [NII] BPT diagrams, SF in the $L_{\mathrm{H}\alpha}$ versus $L_{150\,\mathrm{MHz}}$, and AGN in the WISE color-color diagram, the overall classification of the galaxy is AGN. Any combination that consisted of half SF and half AGN is "unclassified". Similarly, a galaxy is unclassified if it has a combination consisting of the following designations: one AGN, one SF, one intermediate, and one unclassified. In Table 1, we present the number of galaxies and their overall classification for different combinations of the four diagnostic methods of Fig. 1. We show only the combinations that classified at least five galaxies to save space. In each diagnostic diagram, galaxies whose emission is dominated by AGN activity or SF are classified as "AGN" and "SF", respectively. "Int" indicates both AGN activity and SF contribute to galaxy's emission, and "Unc" means that there were no measurements for those galaxies to be classified. In total, there are 380 AGN galaxies, 783 SF galaxies, and 247 unclassified galaxies. From the 380 AGN galaxies, we removed galaxies that had `MANGA_DRP3QUAL` flags indicating that the final cubes and RSS files did not meet qual-

Table 1. Classification of galaxies detected in the MaNGA and LoTSS surveys.

D_n4000 versus $L_{1.4\,\mathrm{GHz}}/M_*$	[NII] BPT	$L_{\mathrm{H}\alpha}$ versus $L_{150\,\mathrm{MHz}}$	WISE color-color	Number of galaxies	Final classification
SF	SF	SF	SF	443	SF
AGN	Unc	SF	AGN	142	AGN
AGN	Int	SF	SF	106	Unc
AGN	SF	SF	SF	87	SF
Unc	Unc	Unc	SF	84	SF
AGN	Unc	SF	SF	79	SF
Unc	Unc	Unc	AGN	61	AGN
AGN	Unc	AGN	AGN	60	AGN
Int	Unc	SF	AGN	42	Unc
SF	Int	SF	SF	39	SF
AGN	AGN	SF	SF	37	Unc
AGN	Unc	Int	AGN	32	AGN
AGN	AGN	SF	AGN	23	AGN
AGN	Unc	Unc	AGN	23	AGN
Unc	Unc	Unc	Unc	21	Unc
AGN	Int	SF	AGN	13	AGN
SF	SF	SF	Unc	10	SF
Int	Int	SF	SF	10	Unc
SF	Unc	SF	SF	10	SF
AGN	Unc	Unc	SF	8	Unc
SF	AGN	SF	SF	7	SF
AGN	Unc	Int	SF	7	Unc
Int	SF	SF	SF	7	SF
SF	Unc	Unc	SF	6	SF
Int	Int	SF	AGN	5	AGN
Int	AGN	SF	SF	5	Unc
Total				380	AGN
Total				783	SF
Total				247	Unc

Table 2. Classification of galaxies in the MaNGA-LoTSS cross catalog.

Diagnostic method	Number classified in MaNGA-LoTSS cross (Number in RDAGN sample)			
	AGN	SF	Intermediate	Unclassified
D_n4000 versus $L_{1.4\,\mathrm{GHz}}/M_*$	633	525	86	166
	(247)	(0)	(11)	49
[NII] BPT	77	555	177	601
	(23)	(0)	(14)	(307)
$L_{\mathrm{H}\alpha}$ versus $L_{150\,\mathrm{MHz}}$	68	1085	46	211
	(52)	(149)	(33)	(73)
WISE color-color	426	942	–	42
	(302)	(2)	–	(3)

ity standards. Additionally, we visually inspected the radio contours and removed galaxies that had no radio emission greater than $3\times$ the rms noise (41 galaxies, see Table A.2). Our final RDAGN sample consists of 307 unique RDAGN-host galaxies. In Table 2, we provide the number of galaxies classified as AGN/SF/intermediate/unclassified in each diagnostic diagram for the entire MaNGA-LoTSS catalog and for the final RDAGN sample. The green, bracketed numbers on the second row for each diagnostic represent the number of galaxies with an overall classification as RDAGN. We provide radio-optical overlays of two of the RDAGN host galaxies in Fig. 2. The example in the top panel of Fig. 2 exhibits radio emission likely powered by both SF and AGN activity. Conversely, the early-type galaxy example (bottom panel of Fig. 2) has two-sided radio jets.
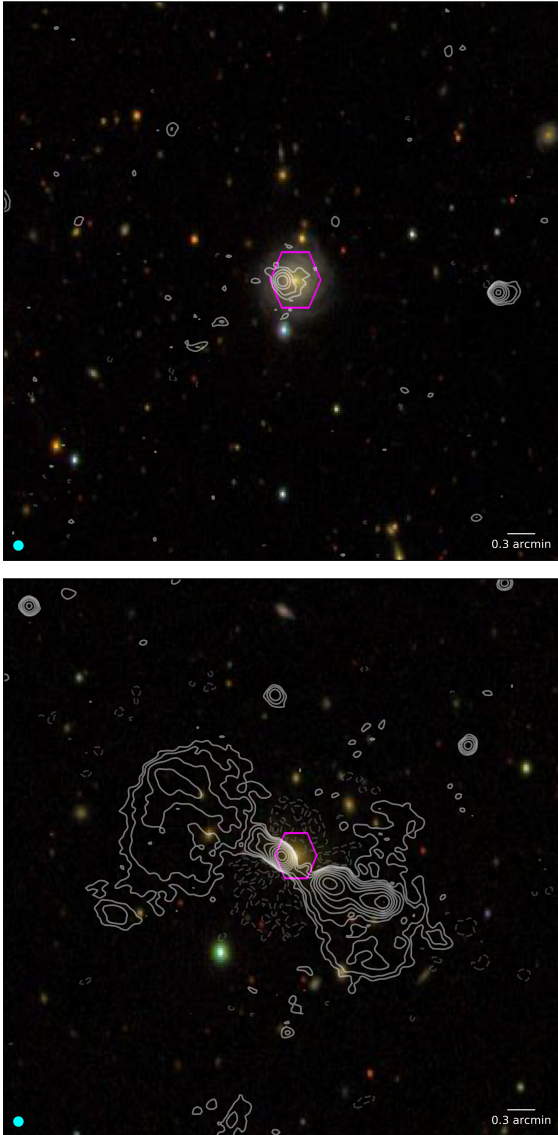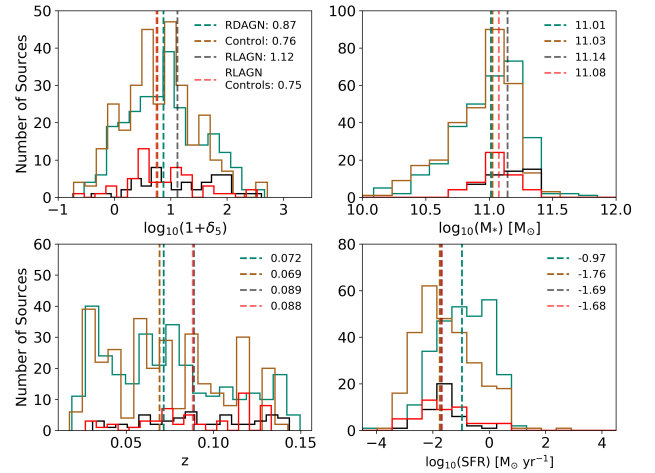
Fig. 3. Distribution of measured properties of the RDAGN (green), control sample (brown), the classical RLAGN (black), and RLAGN control galaxies (red). The median value for each sample is indicated by the dashed, vertical lines. *Top row from left to right*: local galaxy overdensity evaluated at the fifth nearest neighbor (δ_5), M_*. *Bottom row from left to right*: z, SFR as measured by Pipe3D.

Fig. 2. Overlay of LOFAR 150 MHz radio contours on optical SDSS three color image of late-type RDAGN 8978−9101 and early-type RDAGN 8244−6103 (*bottom*). The magenta hexagon represents the MaNGA IFU footprint. Positive contours are defined by rms noise × [3, 6, 12, 24, 48, 96, 192, 384, 768, 1536, 3072]. Negative contours are shown by the gray, dashed line and represent the rms noise × [−3, −6, −12]. The LOFAR beam size is shown in the lower left corner of each image.

3.2. Control sample criteria

From the galaxies in MaNGA DR16 within the LoTSS DR2 footprint, we have selected a control sample of galaxies that closely match the properties of the RDAGN host galaxies except that their nuclei, based on the [NII] BPT and the equivalent width of Hα ($W(\text{H}\alpha)$) versus [NII]/Hα (WHAN; Cid Fernandes et al. 2010) diagrams, are inactive. The control sample was built as follows: First, we selected galaxies whose overall classification was not "AGN" and whose central ionizing source was not AGN. Therefore, we considered a galaxy as a potential control sample candidate if it was in the SF region of the BPT diagram or was classified as a Low-Ionization Emission-line Region (i.e., in the Low-Ionization Nuclear Emission-line Region (LINER; Heckman 1980) region with $W(\text{H}\alpha) < 3$ Å. From these inactive

galaxies, we created a preliminary list of control sample candidates for each RDAGN host, selecting galaxies whose z and M_* did not vary by more than 30% from the RDAGN host's z and M_*. Finally, we selected one control galaxy for each RDAGN host galaxy by visually inspecting the SDSS three color image of each control sample candidate and choosing the galaxy whose morphology and inclination were most similar to the SDSS three color image of the RDAGN host galaxy. Priority was given to morphological features within the MaNGA IFU hexagon footprint. We provide the plateifu identifer for the RDAGN galaxies and their assigned control galaxy in Table A.1.

In some cases, a particular MaNGA galaxy was the best control galaxy for multiple RDAGN samples. For example, although we identify 307 RDAGN galaxies, there are only 157 unique controls. Hence, we use the same best control galaxy more than once so that the total number of RDAGN and controls are equal. To ensure that using the same control galaxy multiple times and visually selecting control galaxies did not affect our results, we performed the analyses presented in Sects. 4 and 6 using the entire non-active galaxy sample (3231 galaxies in total), and found that our results did not change. We chose to use our selected control sample to better understand how RDAGN host galaxies compare to non-active galaxies with similar properties and to overcome potential biases in our SFR measurements (see Sect. 5). In Fig. 3, we show the distribution of properties of the RDAGN sample and of the control sample. By selection, the stellar mass and redshift distributions are the same. Moreover, we find no significant difference in the environment in which these RDAGN and control galaxies reside. Our RLAGN span a large range of stellar mass and radio power based on the distribution of $L_{150\,\text{MHz}}$ provided in Fig. 4.

3.3. Existing MaNGA AGN catalogs

We briefly compare our sample of 307 unique RDAGN to previous studies that have identified AGN in the MaNGA survey, (Rembold et al. 2017; Wylezalek et al. 2018; Sánchez et al. 2018; Comerford et al. 2020). Rembold et al. (2017), Wylezalek et al. (2018), and Sánchez et al. (2018) select
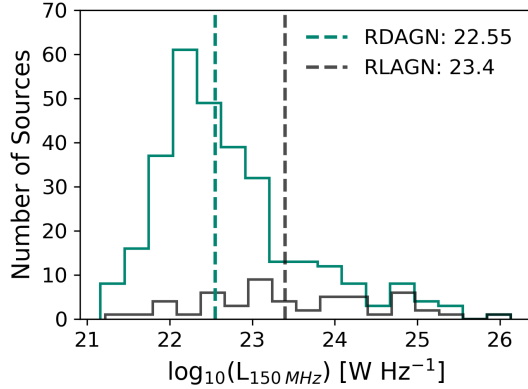
Fig. 4. Distribution of the $L_{150\,MHz}$ for the RDAGN (green) and RLAGN (gray) samples. The median value is indicated by the dashed, vertical line.

AGN using optical emission line ratios and cuts in the EW(Hα). In our sample of 307 RDAGN, 100 (33%) have EW(Hα) > 1.5 Å, and 41 (13%) have EW(Hα) > 3 Å. In the following, we report the percentage of our sample that overlaps with the other MaNGA AGN catalogs and the percentage of our high-EW(Hα) subsample that overlaps. We note, however, that our sample is distinct from these other MaNGA catalogs with RDAGN (e.g., Comerford et al. 2020) because with LOFAR, we are able to detect fainter radio emission from AGN than previously possible. In Fig. 4 we present the distribution of the radio luminosity for our RDAGN sample. The distribution peaks at ∼22.5 W Hz^{-1}, which is lower than the average equivalent 1.4 GHz radio luminosities of radio-AGN in Best et al. (2005b). These lower luminosities are consistent with the results of Sabater et al. (2019), who found many RDAGN at the luminosity range $21 < \log(L_{150\,MHz}$ [W Hz^{-1}]) < 24$ that are only detected with the deeper LoTSS data, and not found in NVSS/FIRST.

3.3.1. Rembold et al. (2017) catalog

Rembold et al. (2017) used SDSS integrated spectra to construct the [NII] BPT diagram (Baldwin et al. 1981) and WHAN diagram to identify "true" AGN in the galaxies observed in the fifth MaNGA Product Launch (MPL-5). Rembold et al. (2017) identify 62 "true" AGN out of the 2778 galaxies (2727 unique galaxies) observed in MPL-5. Of the 62 AGN presented in Rembold et al. (2017), 11 are in our radio-detected AGN catalog (∼4%; 27% with EW(Hα) > 3 Å).

3.3.2. Wylezalek et al. (2018) catalog

Wylezalek et al. (2018) used spatially resolved methods to identify AGN candidates in MPL-5 and determined the classification of each spaxel based on its location on the [NII] and [SII] BPT diagrams. Their sample consists of 308 "AGN candidates" that have a high spaxel fraction of AGN in both the [NII] and [SII] BPT diagrams and have cuts on the equivalent width and surface brightness of Hα. 28 AGN candidates from Wylezalek et al. (2018) are in our AGN catalog (∼9%; 32% with EW(Hα) > 3 Å).

3.3.3. Sánchez et al. (2018) catalog

Sánchez et al. (2018) chose AGN using Pipe3D's integrated emission-line ratios within the central 3″×3″ of MPL-5 galaxies.

They classified galaxies as AGN if their integrated emission-line ratios were above the [NII] BPT maximum starburst line from Kewley et al. (2001) and whose W(Hα) was greater than 1.5 Å. Sánchez et al. (2018) identified 98 AGN from the 2700 galaxies in MPL-5, 22 of which overlap with our RDAGN sample (∼7%; 19% with EW(Hα) > 1.5 Å).

3.3.4. Comerford et al. (2020) catalog

Comerford et al. (2020) selected AGN in galaxies observed in MPL-8 using broad Balmer emission lines from SDSS DR7 spectra, radio observations from NVSS (Condon et al. 1998) and FIRST (Becker et al. 1995), WISE mid-infrared colors, and ultra-hard X-ray observations from the *Swift* observatory's Burst Alert Telescope (BAT). Comerford et al. (2020) used the SDSS DR7 AGN catalog from Best & Heckman (2012) to identify radio AGN in MaNGA MPL-8. Best & Heckman (2012) selected radio AGN using the D_n4000 versus $L_{1.4\,GHz}/M_*$, [NII] BPT diagram, and $L_{H\alpha}$ versus $L_{150\,MHz}$. Unlike the WISE diagnostic methods presented in this study, Comerford et al. (2020) follow Assef et al. (2018), adopting the 75% reliability criteria of $W1-W2 > 0.486e^{0.092(W2-13.07)^2}$ and $W2 > 13.07$, or $W1-W2 > 0.486$ and $W2 \leq 13.07$. Of the 6261 galaxies observed in MPL-8, Comerford et al. (2020) identify 406 unique AGN. Comerford et al. (2020) focused their analyses on comparing 81 radio-quiet galaxies undetected in the radio with 143 radio-mode AGN. 52 AGN from Comerford et al. (2020) are in our AGN catalog (∼17% of our sample, or ∼13% of their total AGN and 38% of their RDAGN sample).

3.4. Comparison of global properties

We show SFR as a function of M_* for our sample of RDAGN, as well as for those AGN in other MaNGA AGN catalogs outlined above in Fig. 5. Compared to optically selected AGN catalogs (Rembold et al. 2017; Sánchez et al. 2018; Wylezalek et al. 2018), radio-selected AGN (Comerford et al. 2020, and this study) have a strong tendency to occupy massive host galaxies. This is already a well observed trend (e.g., Gürkan et al. 2018; Sabater et al. 2019) and indicates that radio-AGN selection intrinsically selects for a different population of host galaxies (i.e., massive early-type galaxies – hereafter ETGs – for radio-AGN, and less massive late-type galaxies – hereafter LTGs – for optically selected AGN). Figure 5 illustrates that galaxies experiencing quenching (Green Valley galaxies) and AGN host galaxies share a similar location on the SFR$_*$ plane, which is also well observed (e.g., Sánchez et al. 2018; Lacerda et al. 2020).

4. Relation to the star-forming main sequence

Star-forming galaxies fall on a tight correlation (∼0.2 intrinsic scatter; Speagle et al. 2014) between SFR and M_*, known as the main sequence (Brinchmann et al. 2004; Daddi et al. 2007; Elbaz et al. 2007; Noeske et al. 2007). Previous studies have found that AGN add additional complexity to the regulatory processes of SF when compared to non-active galaxies of comparable mass. For example, Mullaney et al. (2015) and Shimizu et al. (2015) have found that the SFRs in X-ray-selected AGN host galaxies have more suppressed SFRs than non-active galaxies of similar mass, whereas Young et al. (2014) and Pitchford et al. (2016) have found that quasar host galaxies have higher SFRs than comparably massive, non-active galaxies. Moreover, the type of AGN – such as radio-quiet or radio-loud,
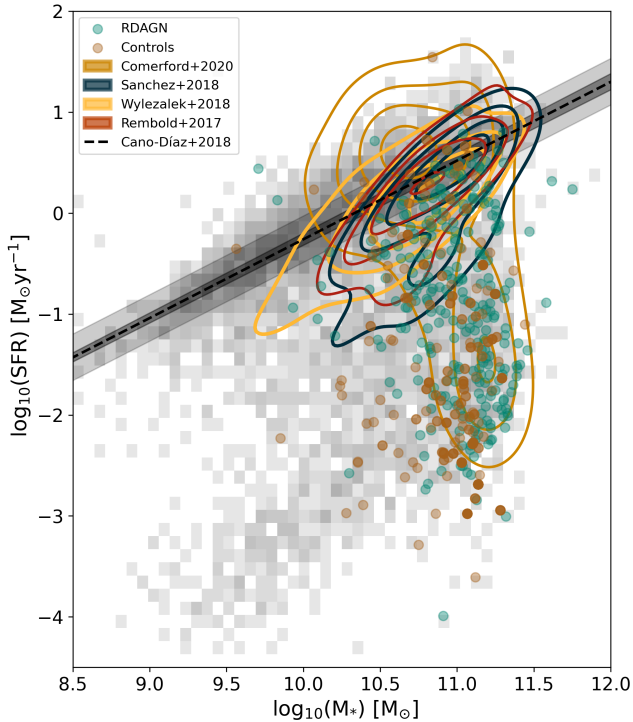
Fig. 5. Relation between SFR and M_* for existing MaNGA AGN catalogs. The gray-colored image represents the density of MaNGA galaxies in the plot. The RDAGN studied in this work are indicated in green. Dark yellow contours represent the density of AGN host galaxies for from the Comerford et al. (2020) AGN catalog, the dark blue contours represent the density of galaxies from the Sánchez et al. (2018) AGN catalog, the Wylezalek et al. (2018) AGN catalog are represented by orange contours, and the red contours exhibit the density of Rembold et al. (2017) AGN catalog. The SFR–M_* space is divided into 50×50 bins, and the contours are drawn at 25, 50, 75, and 100% of the maximum number density. The dotted line represents the SFMS derived for SDSS-IV MaNGA galaxies derived by Cano-Díaz et al. (2019), the dark gray shading represents the errors on slope, and the light gray shading represents the standard deviation.

LERGs or HERGs – that a galaxy hosts appears to influence the SFRs (e.g., Hardcastle et al. 2013; Heckman & Best 2014; Ellison et al. 2016; Magliocchetti et al. 2016, 2018; Roy et al. 2018; Comerford et al. 2020).

In this section, we show the relation of RDAGN host galaxies and control galaxies to the SFMS using the integrated stellar mass and SFR from the Pipe3D VAC. In Fig. 6, we show the correlation between SFR and M_* for the full sample and for AGN subsamples based on the diagnostic diagrams used in Sect. 3.1 and based on morphology. We include the SFMS relation derived for SDSS-IV MaNGA galaxies from Cano-Díaz et al. (2019), which is defined by $\log(\mathrm{SFR}/M_\odot\,\mathrm{yr}^{-1}) = -8.06 \pm 0.04 + (0.78 \pm 0.01) \times \log(M_*/M_\odot)$ and has a standard deviation of 0.23. Additionally, we show the best-fit relation for radio-quiet and radio-mode MaNGA AGN derived by Comerford et al. (2020). These lines are defined as $\log(\mathrm{SFR}/M_\odot\,\mathrm{yr}^{-1}) = \alpha + \beta\log(M_*/M_\odot)$, where $\alpha = -88.1 \pm 8.1$ and $\beta = 7.7 \pm 0.7$ for radio-mode AGN and $\alpha = -21.5 \pm 0.7$ and $\beta = 2.01 \pm 0.06$ for radio-quiet AGN.

We present the M_*–SFR function for our RDAGN and control samples in Fig. 6 and find that both the RDAGN sample and the control sample typically lie below the main sequence. To confirm the observed similarity between the two samples, we calculated the distance from the SFMS ($\Delta \log_{10}(\mathrm{SFR})$) by sub-

tracting the (logarithmic) SFR of the SFMS from the SFR of the sample ($\Delta \log_{10}(\mathrm{SFR}) = \log_{10}(\mathrm{SFR}_{\mathrm{sample}}) - \log_{10}(\mathrm{SFR}_{\mathrm{SFMS}})$). We present these values in the left-most column of Table 3. All error values presented in Table 3 represent the standard deviation. Although the median $\Delta \log_{10}(\mathrm{SFR})$ of the RDAGN sample ($-1.51\,\mathrm{dex} \pm 3.20$) lies closer to the SFMS than the median of the control sample ($\Delta \log_{10}(\mathrm{SFR}) = -2.29\,\mathrm{dex} \pm 3.03$), the standard deviation errors on the median overlap. Therefore, the difference between the median $\Delta \log_{10}(\mathrm{SFR})$ at a fixed stellar mass for the RDAGN sample and the control sample is not statistically significant (see Table 3).

RDAGN classified as "AGN" in the [NII] BPT diagram and those residing in LTGs tend to agree with the best-fit relation for radio-quiet AGN of Comerford et al. (2020) (median $\Delta \log_{10}(\mathrm{SFR}) \sim -0.359$ and -0.465, respectively). This is expected as the BPT diagram tends to select radiatively efficient AGN, which are typically radio quiet. Furthermore, radio quiet AGN are often hosted by LTGs.

Conversely, we find that early-type RDAGN and RDAGN classified as "AGN" on the $L_{\mathrm{H}\alpha}$ versus $L_{150\,\mathrm{MHz}}$ typically agree with the best fit relation for radio-mode AGN (Comerford et al. 2020, median $\Delta \log_{10}(\mathrm{SFR}) \sim -1.74$ and -2.35, respectively). This is again expected as the selection criterion $L_{\mathrm{H}\alpha}$ versus $L_{150\,\mathrm{MHz}}$ selects radio loud objects, and radio-loud AGN typically reside in ETGs.

We have found that the majority of the RDAGN lies below the SFMS, which is consistent with what is expected for the position of radio AGN relative to the main sequence (e.g., Gürkan et al. 2018). Unlike previous studies (e.g., Young et al. 2014; Mullaney et al. 2015; Shimizu et al. 2015; Leslie et al. 2016; Pitchford et al. 2016), which found that AGN host galaxies have different SFRs than non-active galaxies of similar mass, we find no statistically significant difference between the SFR of the RDAGN sample and the control sample selected by mass and morphology. This result compliments the findings presented in previous explorations of AGN feedback with MaNGA (e.g., Sánchez et al. 2018) and with the CALIFA survey (Calar Alto Legacy Integral Field Area; e.g., Lacerda et al. 2020), specifically that there is no significant difference between the properties of galaxies in the Green Valley hosting an AGN and those without an AGN. Our results indicate that the RDAGN, selected based on their current activity, are not responsible for any quenching that has taken place in their host galaxies. The mechanism or mechanisms responsible for suppressing SF must be related to the host galaxy's properties (i.e., the fact that these are preferentially ETGs, with lower SF than star forming galaxies), which is in agreement with the burgeoning literature that the growth of galactic bulges, AGN activity, and the halting of SF appear to occur concomitantly (e.g., Lacerda et al. 2020, and references therein).

Toward understanding how the SFRs between each RDAGN and its assigned control galaxy directly compare, we look at the fractional difference of Pipe3D's SFR measurement, which is the difference between the SFR of the RDAGN and its control divided by the SFR of the RDAGN (($\mathrm{SFR}_{\mathrm{AGN}} - \mathrm{SFR}_{\mathrm{Control}})/\mathrm{SFR}_{\mathrm{AGN}}$). Dividing the difference by the SFR of the RDAGN helps scale the range of measured SFRs. When the fractional difference is positive, it means that the RDAGN host galaxy has a higher SFR than its assigned control galaxy. Conversely, when the difference is negative, the control galaxy has a higher SFR. We present the distribution of the fractional difference in Fig. 7.

In Fig. 7, the fractional difference of the SFR between the RDAGN sample and control sample is represented by
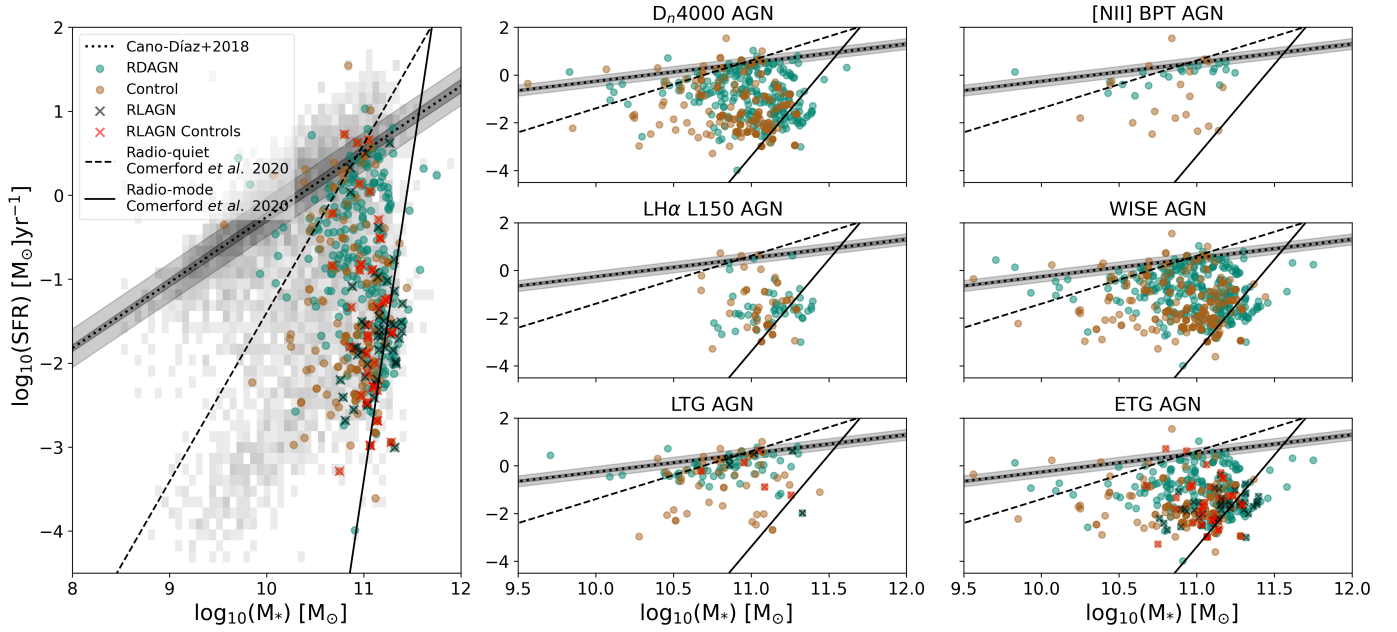
Fig. 6. Relation between SFR and M_* for RDAGN host galaxies (green), the full control sample (brown), RLAGN subsample (black x's), RLAGN control galaxies (red x's), and entire Pipe3D catalog (gray). For reference, the SFMS derived for SDSS-IV MaNGA galaxies is indicated by the dotted line (Cano-Díaz et al. 2019), the dark gray shading represents the errors on slope, and the light gray shading represents the standard deviation. The best-fit relations for radio-quiet AGN (dashed line) and radio-mode AGN (solid line) are from Comerford et al. (2020).

Table 3. Median distance from the SFMS (left), and the average light-weighted age gradient (right).

Sample	Median $\Delta \log_{10}(SFR)$	Median α
RDAGN	-1.51 ± 3.20	-0.097 ± 0.226
Full control	-2.29 ± 3.03	-0.100 ± 0.221
RLAGN	-2.35 ± 3.15	-0.09 ± 0.211
RLAGN controls	-2.38 ± 1.75	-0.11 ± 0.186
D_n4000 versus $L_{1.4\,GHz}/M_*$ AGN	-1.52 ± 3.31	-0.093 ± 0.217
[NII] BPT AGN	-0.359 ± 3.37	-0.128 ± 0.211
$L_{H\alpha}$ versus $L_{150\,MHz}$ AGN	-2.35 ± 3.15	-0.092 ± 0.211
WISE color-color AGN	-1.51 ± 3.22	-0.094 ± 0.224
LTG AGN	-0.465 ± 3.47	-0.263 ± 0.238
ETG AGN	-1.74 ± 3.09	-0.075 ± 0.201

the distribution shaded in green. We find that ∼44% of the RDAGN-control pairs exhibit a positive fractional difference. The percentage increases when late-type AGN host galaxies are considered; ∼51% of the RDAGN LTGs have higher SFRs than the corresponding controls. Finally, for the ETGs, only ∼43% of the RDAGNs have higher SFRs. For classical RLAGN and their corresponding control galaxies, we discover a higher percentage of positive fractional differences. The full RLAGN sample and the early-type RLAGN subsample express a similar percentage (∼54%) of positive fractional differences. We find that ∼80% of late-type RLAGN express a positive fractional difference.

Our fractional difference of SFR results are both agree and disagree with those of do Nascimento et al. (2019; a MaNGA AGN study that uses the Rembold et al. 2017 catalog). We note that the SFR measurements that do Nascimento et al. (2019) use in their fractional difference analysis were taken using similar methods outlined in Sect. 5.2. We chose to use Pipe3D's values instead of the ones we calculate in Sect. 5.2 in order to have a SFR measurement for each RDAGN and control galaxy (discussed further at the beginning of Sect. 5). Nevertheless, both

do Nascimento et al. (2019) and Pipe3D measure SFR using the extinction-corrected $L_{H\alpha}$ equation from Kennicutt (1998; see Eq. (1)) facilitating comparison.

Whereas do Nascimento et al. (2019) find that 76% of ETG AGN have higher SFRs than their assigned control galaxies, only ∼43% of our RDAGN ETG host galaxies have higher total SFRs than their controls. Our values agree more when comparing the percentage of positive fractional differences in the early-type RLAGN sample (∼54%). We believe that the difference in our percentages and those reported by do Nascimento et al. (2019) is due the differences in our AGN samples.

Interestingly, we discover that ∼51% of our late-type RDAGN host galaxies have higher total SFRs than their controls, which is the same percentage reported by do Nascimento et al. (2019). This might be a sign either of positive feedback playing a role at earlier stages of a galaxy's evolution or that LTGs simply have more availability of fuel. To distinguish between these two scenarios, we would need to prove that radio jet activity is physically reaching regions where SF is occurring.

5. Spatially resolved stellar and nebular gas properties

5.1. Ionization classification maps

A galaxy's spectrum contains a wealth of information that is used to infer the physical processes taking place within the galaxy. Historically, the dominant excitation mechanism of a galaxy was inferred using single-aperture spectroscopy (e.g., Kauffmann et al. 2003; Kewley et al. 2006, and references therein). However, with IFS data, multiple ionizing sources can be determined and spatially mapped because a spectrum of light is measured at every spatial pixel observed with the IFU. Here, we optically classify the spaxels of the RDAGN and control galaxies to separate multiple ionizing sources and to gauge the frequency of these mechanisms at three different galactocentric

Table 4. Dominant ionizing mechanism at 0.2, 0.6 and 1.0 R_e.

R/R_e	RDAGN (%)			Controls (%)			LTGs (%)			ETGs (%)		
	0.2	0.6	1.0	0.2	0.6	1.0	0.2	0.6	1.0	0.2	0.6	1.0
HII	0	0.33	1.95	2.28	4.23	7.82	0	0	7.69	0	0.41	0.41
Composite	5.86	7.82	11.7	2.93	5.21	4.56	7.69	20.0	38.5	5.37	4.55	4.55
LINER	6.51	2.93	1.63	0	0	0	15.4	4.62	3.08	4.13	2.48	1.24
Seyfert	0.98	0.98	0.65	0	0	0	3.08	3.08	1.54	0.41	0.41	0.41
LIER	85.7	87.3	83.39	92.5	89.9	87.0	69.2	72.3	49.23	86.4	91.3	92.6
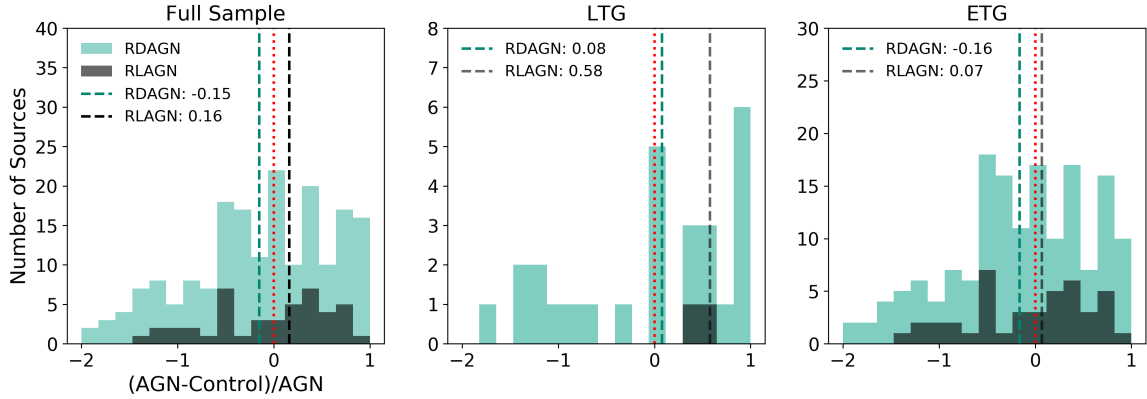
Fig. 7. Distribution for the fractional difference in the SFR as measured by Pipe3D of the RDAGN and its control galaxy for the entire sample, LTGs, and ETGs (green shading). The same values are also shown for the classical RLAGN subsample and its controls (black shading). The vertical, dashed lines represent the median of the distribution. A one-to-one line at zero is represented by the red, dotted line.

radii. Knowing where the gas is being excited by these mechanisms is important for obtaining accurate SFR from the luminosity of Hα, which is the approach used in Sect. 5.2.

Emission-line fluxes across the surface for each galaxy were obtained using the Maps galaxy tool from SDSS Marvin (Cherinka et al. 2019). We determined the S/N of each 2D map using the get_snr() function. We also masked spaxels at six wavelengths (Hβ λ4862, [OIII] λ5008, [NII] λ6585, Hα λ6564, [SII] λ6718, 6732) that contained negative flux values as well as those that had a S/N less than 3 using the get_masked() function. In addition to the emission-line fluxes, we obtained the equivalent width of Hα line (W(Hα)) to construct the W(Hα) versus [NII]/Hα (WHAN) diagram and measurements of the elliptical radius in order to determine the excitation mechanisms within the nuclear region of each galaxy.

To determine the excitation mechanism of each spaxel we combined information obtained from three diagrams: the [NII] BPT diagram, [SII] BPT diagram, and the WHAN diagram. Figure 8 shows an example of the classification methods combined to create the ionization classification map (bottom right) for RDAGN galaxy, 8978−9101. Using the emission-line fluxes at each spaxel, we measured the ratio of [NII] to Hα, [SII] to Hα, and [OIII] to Hβ. To determine whether the excitation mechanism was from starburst activity/young hot stars (HII) or "composite", meaning that the gas is likely being excited by a blend of AGN activity and SF, we used the [NII] BPT diagram and its diagnostic lines. In Fig. 8, the [NII] BPT diagram is shown in the upper left panel. The points colored brown and beige represent the spaxels of RDAGN 8978−9101 whose excitation mechanism is SF and composite, respectively. The points colored gray, represent spaxels whose emission is likely powered by AGN activity.

The [SII] BPT diagram was used to distinguish emission line regions dominated by Seyfert-like and LINER-like exci-

tation. We chose the [SII] BPT (upper right corner of Fig. 8) to separate these ionizing mechanisms because the low ionization potential of the [SII]/Hα reveals the low ionization emission lines of LINER spectra better than [NII]/Hα. Consequently, the Seyfert-LINER demarcation is more robust on the [SII] BPT than on the [NII] BPT (Kewley et al. 2006). The solid line on the [SII] BPT represents the demarcation between HII excitation from AGN excitation and it is defined by log([OIII]/Hβ) = 0.72/(log([SII]/Hα) − 0.32) + 1.30 (Kewley et al. 2001), where every spaxel above the line is dominated by AGN activity and SF below the line. Seyfert-like excitation is separated from LINER-like excitation by the line log([OIII]/Hβ) = 1.89 × log([SII]/Hα) + 0.76 (Kewley et al. 2006), which is shown by the dotted line on the [SII] BPT diagram in Fig. 8. All spaxels that fall above this line are classified as Seyfert and spaxels are classified as LINER if they are below the line. In the [SII] BPT, spaxels whose excitation mechanism is Seyfert-like are colored green and those spaxels with LINER-like excitation are colored light green.

There are multiple ionizing mechanisms that are connected to LINER-like emission in galaxies. Those mechanisms include shock ionization, a weak AGN, or photo-ionization from hot, evolved stars (e.g., post-asymptotic giant branch stars (pAGB); Binette et al. 1994; Stasińska et al. 2006; Sarzi et al. 2010; Cid Fernandes et al. 2011; Yan & Blanton 2012; Belfiore et al. 2016, and references therein). IFU surveys such as CAL-IFA and MaNGA have revealed that LINER-like emission-line ratios can be seen throughout galaxies (e.g., Singh et al. 2013; Belfiore et al. 2016), which is attributed the extended LINER-like emission from pAGB stars, which is known as Low-Ionization Emission line Region-like (LIER) excitation (see Gomes et al. 2016; Lacerda et al. 2018; Espinosa-Ponce et al. 2020, for a more detailed exploration of the pAGB origin of
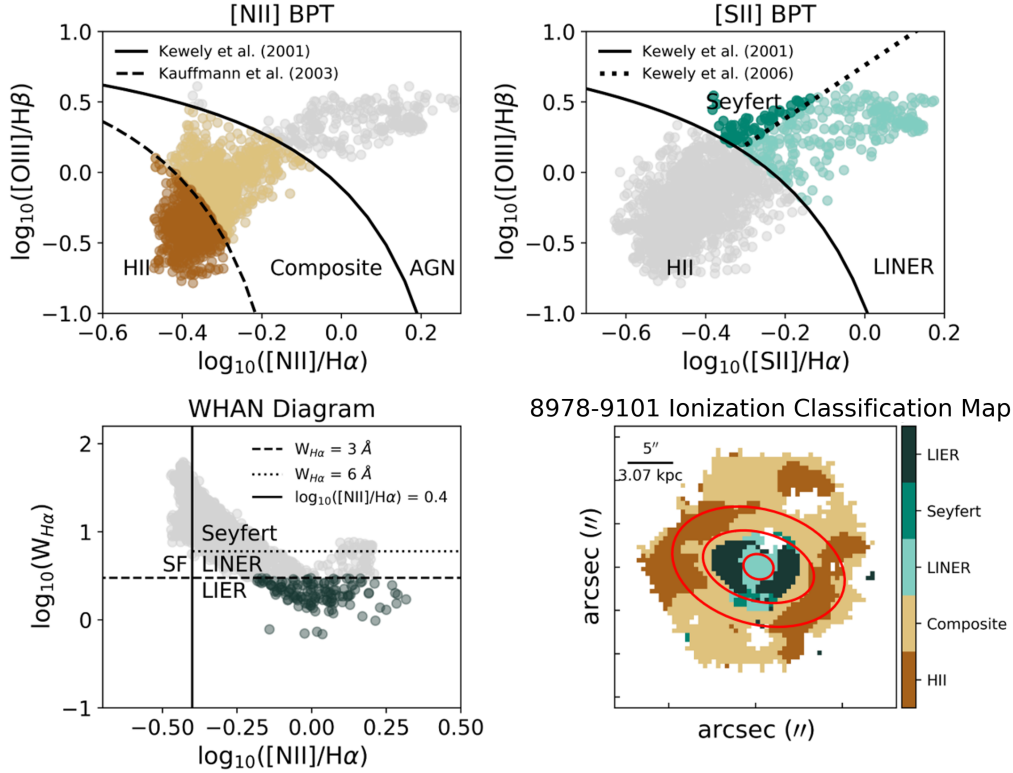
Fig. 8. Example of the diagrams used to determine the gas excitation mechanisms across the surface of each galaxy. Each point on the diagrams represents a spaxel. *Top row from left to right*: [NII] BPT diagram and [SII] BPT diagram of a late-type RDAGN galaxy example. The solid line represents the maximum starburst line from Kewley et al. (2001). The dashed line on the [NII] BPT diagram represents the Kauffmann et al. (2003) line, which separates pure SF galaxies from composite galaxies. The dotted line on the [SII] BPT diagram separates Seyfert-like excitation from LINER-like excitation (Kewley et al. 2006). *Bottom row from left to right*: WHAN diagram and final ionization classification map of RDAGN galaxy 8978−9101. The [NII] BPT was used to separate HII (brown) and composite (beige) excitation, the [SII] diagram was used to distinguish Seyfert-like excitation (green) from LINER-like excitation (light green), and the WHAN diagram was used to differentiate LIER-like excitation (dark green) from LINER-like excitation. The red ellipses represent, from the inside outward, $0.2\,R/R_e$, $0.6\,R/R_e$, $1\,R/R_e$.

diffuse ionization in galaxies). To separate LIER-like excitation from LINER-like excitation, we constructed the WHAN diagram (lower left panel of Fig. 8). Several lines of demarcation appear on the WHAN diagram: the solid, vertical line at $\log_{10}([NII]/H\alpha) = -0.4$ separates SF (left) from AGN/non-SF activity (right), the dotted, horizontal line separates Seyfert-like excitation from LINER-like excitation, and the dashed, horizontal line separates LIER-like excitation from LINER-like excitation. Points colored dark green on the WHAN diagram in Fig. 8 represent the spaxels in RDAGN 8978−9101 with LIER-like excitation.

After the dominant ionizing mechanism was determined for each spaxel, we spatially mapped (see lower right panel in Fig. 8) the excitation mechanisms. The ionization classification maps for RDAGN 8978−9101 and RDAGN 8244−6103, are compared to those of their controls in Fig. 9. In the LTG example (RDAGN 8978−9101, top panel of Fig. 9), both the RDAGN host galaxy and the control are dominated by spaxels consistent with HII excitation (brown) and by composite emission (beige). In the central 5″, there is LIER (dark green) and LINER-like (light green) excitation, likely from pAGB stars and from a weak AGN, respectively. Conversely, the spaxels in the ETG example (RDAGN 8244−6103, see Fig. 9) are mostly classified as LIER (dark green), which likely correspond to their old stellar populations.

It is important to emphasize that although we have separated "HII" and "Composite" spaxels, in IFS data, gas with both HII

and composite emission line ratios is most likely excited by SF. This is why, in Sect. 5.2, we calculate SFRs from the Balmer lines in both HII and composite spaxels. We should also keep in mind that shocks can reproduce line ratios that are typical for the HII, Composite, to the Seyfert and LINER regions of the diagnostic diagrams (e.g., Allen et al. 2008). Future work to identify shocks from mergers or outflows driven by toward or AGN activity in our sample will require a combination of emission line analysis with spatial and velocity information (e.g., López-Cobá et al. 2019, 2020).

In Fig. 10 we provide line graphs, which display the percentage of galaxies that have HII, Composite, LINER, Seyfert, and LIER at 0.2, 0.6, and 1.0 effective radius (R_e) as the dominant excitation mechanism and provide the numerical values in Table 4. When the percentage equals 0, it indicates that the specific ionizing mechanism is not the dominant type at the given R_e. Before elaborating further on these results, some samples appear to not have certain spaxel-types (i.e., 0%). To be clear, that does not mean that the specific excitation mechanism does not occur in that given galaxy. Instead, it means that the excitation type was not the dominant ionizing mechanism (i.e., by number of spaxels) within the radial bin of 0.2, 0.6, or 1.0 R_e.

We find that within $0.2\,R_e$ of each galaxy (i.e., the nuclear region), LIER-like excitation (represented by the dark green line in Fig. 10) is the most common ionizing mechanism in all samples. ~85% of RDAGN galaxies and ~93% of control galaxies exhibit LIER spaxels near the nuclear region. Approximately

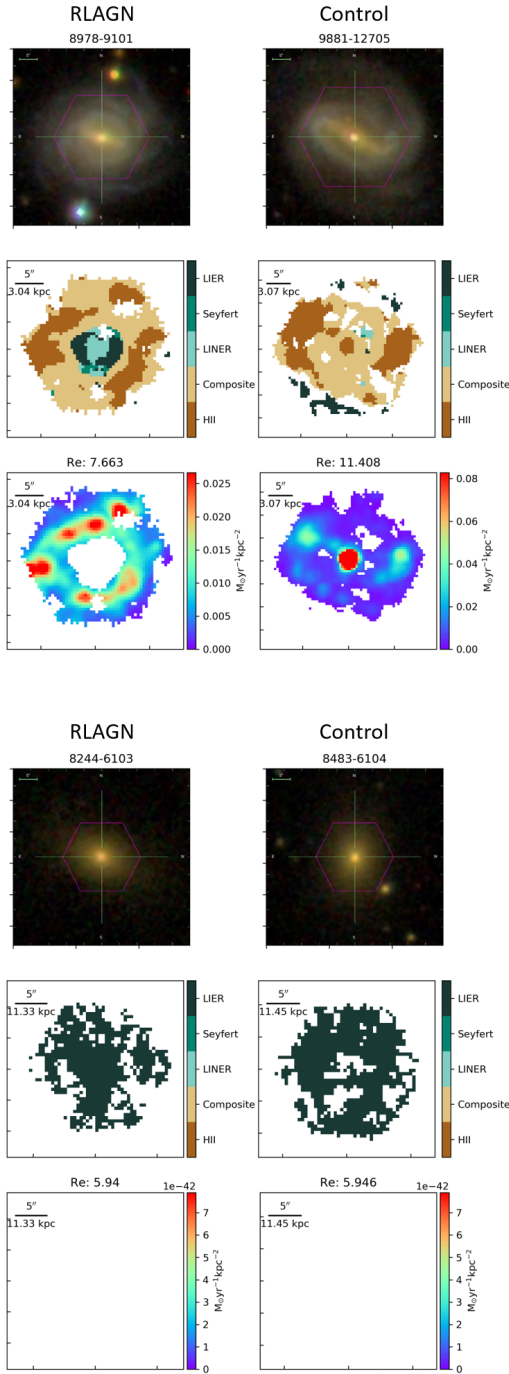**Fig. 9.** Surface distribution of gas excitation mechanisms (*middle panel*) and $\sum$SFR (*bottom panel*) for late-type RDAGN 8978−9101 and its control galaxy 9881−12705 (*top*) and early-type RDAGN 8244−6103 and its control galaxy 8483-6104 (*bottom*). For the early-type RDAGN and its control, the $\sum$SFR maps are blank because those galaxies do not contain SF or composite spaxels. The optical SDSS image overlaid with the MaNGA IFU footprint (magenta hexagon) is shown on the top panel of the figure.

69% and 86% of LTGs and ETGs galaxies are dominated by as LIER spaxels in the nuclear region, respectively. At larger effective radii, LIER spaxels become less common (varies between ~83−85% for the entire RDAGN sample and ~87−92% for the control sample), but still remain the dominant excitation mechanism. In the RDAGN sample and the subsample of early-

type AGN host galaxies, the percentage of galaxies dominated by LIER spaxels peaks at $0.6\,R/R_e$ (~87%). The presence of LIER-like emission throughout the entire galaxy, regardless of activity or morphology, is consistent with previous studies (e.g., Singh et al. 2013; Gomes et al. 2016; Belfiore et al. 2016; Wylezalek et al. 2018). Although pAGB stars are likely responsible for the photoionziation of gas in these spaxels, another possible interpretation of the LIER emission is that it is a relic ionization signature from an AGN that has recently stopped accreting material and has "turned off" (e.g., Papaderos et al. 2013; Gomes et al. 2016; Schirmer et al. 2016; Keel et al. 2017; Ichikawa et al. 2019).

Galaxies dominated by composite spaxels (represented by the beige line in Fig. 10) are the next most common type. In the RDAGN sample and the late-type RDAGN host galaxy subsample, the percentage of composite spaxel-dominated galaxies increases with increasing distance from the center of the galaxy. We find that the fraction of LTGs dominated by composite spaxels exhibits the largest increases in frequency with radius (~31% from 0.2 to $1.0\,R_e$). In the control sample, the percentage of galaxies dominated by composite-like excitation peaks at $0.6\,R/R_e$ (5.21%).

Compared to the entire control galaxies, we find that there are fewer RDAGN dominated by HII excitation (illustrated by the brown line in Fig. 10). This could indicate that these RDAGN galaxies are more quenched than the control galaxies.

We find that only RDAGN exhibit LINER spaxels (light green colored line in Fig. 10) and that the percentage of galaxies dominated by this excitation mechanism decreases with increasing R/R_e (~6.5% to ~1.6% from 0.2 to $1.0\,R/R_e$).

Similar trends are observed for RDAGN galaxies dominated by Seyfert spaxels (mid-green line in Fig. 10, although at smaller percentages than LINER spaxels (remains <1%)). It is not surprising that we do not find any Seyfert or LINER dominated control galaxies because our selection excluded galaxies dominated by LINER and Seyfert excitation in the central 3″ of the SDSS fiber (see Sect. 3.2).

5.2. SFR surface density ($\sum$SFR)

In order to obtain the SFR surface density $\sum$SFR), we calculated the SFR in each spaxel using the extinction-corrected $L_{H\alpha}$ equation from Kennicutt (1998):

$$\sum \text{SFR} = 7.9 \times 10^{-42} \times L(\text{H}\alpha), \tag{1}$$

where $L(\text{H}\alpha)$ is in units of erg s^{-1}. We correct Hα emission for extinction ($\lambda = 6563\,\text{Å}$) in magnitudes calculated by Cardelli et al. (1989):

$$A_\lambda = A_V \left(a + \frac{b}{2.87} \right), \tag{2}$$

where A_V is derived by comparing the ratio of extinction for the observed fluxes of Hα ($F(\text{H}\alpha)$) and Hβ ($F(\text{H}\beta)$) to theoretical intrinsic value from case B recombination of Osterbrock & Ferland (2006):

$$A_V = 7.23 \times \log \left[\frac{F(\text{H}\alpha)}{F(\text{H}\beta)} \times \frac{1}{2.87} \right]. \tag{3}$$

From there, we calculated the extinction-corrected $F(\text{H}\alpha)$ ($F(\text{H}\alpha)_0$ in units $10^{-17}\,\text{erg s}^{-1}\,\text{cm}^{-2}\,\text{spaxel}^{-1}$)

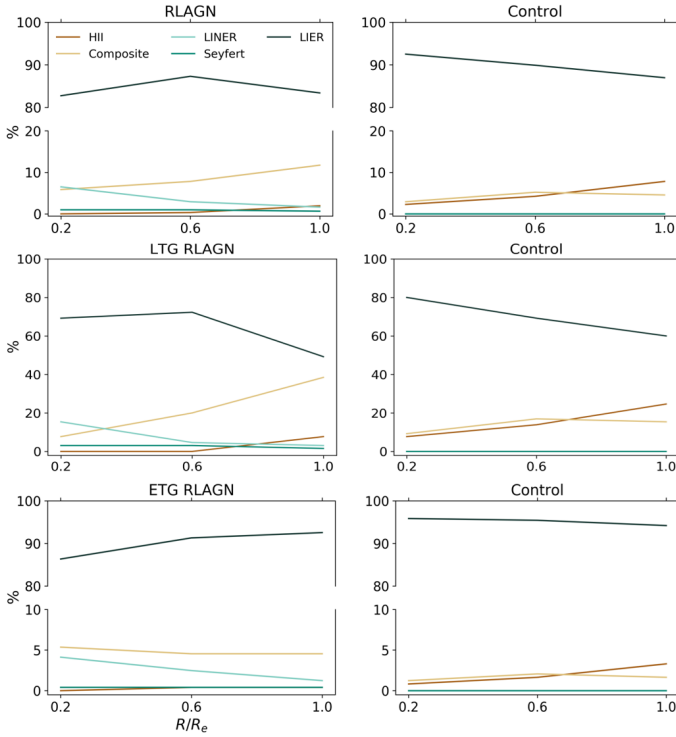$$F(\text{H}\alpha)_0 = F(\text{H}\alpha) \times (10^{0.4 A_\lambda}), \tag{4}$$

Fig. 10. Percentage of galaxies that have emission typical of SF, Composite, LINER, Seyfert, and LIER activity within 0.2, 0.6, and 1.0 effective radius (R_e) from the nucleus of the galaxy. We use a broken y-axis for the top and bottom rows.

and finally the extinction-corrected $L(H\alpha)$

$$L(H\alpha) = 1 \times 10^{-17} \times F(H\alpha)_0 \times 4\pi d_{cm}^2, \qquad (5)$$

where d_{cm} is the luminosity distance in centimeters at the redshift of each galaxy, calculated using Astropy's[3] function cosmo.luminosity_distance(). To convert the angular size of each spaxel to physical size, we calculated the following scale-factor using the small angle approximation and the galaxy's luminosity distance in kpc, d_{kpc}. The area of the spaxel was then determined by multiplying the scaling relation by the angular size of the spaxel (0.5″ for MaNGA IFU) squared. Finally, after calculating the SFR in HII and composite spaxels, we divided each spaxel by its physical size to obtain the $\sum$SFR.

In the bottom panels of Fig. 9, we present the surface distribution of the $\sum$SFR. Unlike the spatial maps for the late-type RDAGN example and its assigned control galaxy, the maps for the early-type RDAGN host and control are blank. This is expected because neither the early-type RDAGN host galaxy nor its control contained HII or composite spaxels.

In Fig. 11, we present histograms for the median $\sum$SFR and total SFR (sum of SFR across every spaxel) for the RDAGN sample and control sample and for samples subdivided according to morphology. To the left of the black vertical line, these quantities were derived using all spaxels with a $S/N > 0$, and to the right of the line, only HII and composite spaxels with a $S/N > 3$. We show the results from these different scenarios to gauge whether or not our choice to measure the SFR spaxels with HII and composite spaxels affected our final result. We report a statistically significant difference between the median $\sum$SFR of

the RDAGN and the control sample when all spaxels are considered, but no difference in the total SFRs. The RDAGN show higher median $\sum$SFR than the control sample ($\sum$SFR = $10^{-2.56}$ compared to $10^{-4.35}$ $M_\odot$ yr^{-1} kpc^{-2}), which could indicate either that there are regions with enhanced SFR within our RDAGN (signs of positive feedback) or that calculating SFRs from Hα in these cases is not reliable. We interpret these results as confirmation of our choice to measure the SFR in HII and composite spaxels. We chose not to show the RLAGN subsample on these panels because there are too few galaxies in the sample for any differences in the $\sum$SFR and total SFR between the AGN host galaxies and the control galaxies to be called statistically significant.

When considering HII and Composite spaxels with $S/N > 3$, we find that the average $\sum$SFR for RDAGN galaxies is -2.36 in logarithmic units of $M_\odot$ yr^{-1} kpc^{-2}, which is higher than the controls' value of -2.41. We find that the total SFR for RDAGN ranges between $\sim 10^{-4.23}$ $M_\odot$ yr^{-1} and $10^{1.09}$ $M_\odot$ yr^{-1}. The total SFR of the controls range from $\sim 10^{-5.25}$ to $10^{1.21}$ $M_\odot$ yr^{-1}.

Toward assessing the probability that the RDAGN sample and the control sample were drawn from the same parent population, we performed a two-sample Anderson-Darling (A−D) test. When the A−D statistic is less than the critical value at the specified significance level, the null hypothesis – that the $\sum$SFR RDAGN sample and the control sample were drawn from the same distribution – cannot be rejected in favor of the alternative hypothesis, which is that the distributions of the two samples are different. Before performing the test, we set the reference significance level to 0.05. For the $\sum$SFR of entire RDAGN and control samples, which is presented in the top panel of Fig. 11, the A−D statistic is ~ 0.08, which is less than the critical value at $p = 0.05$ (~ 4.59). Therefore, the null hypothesis is not rejected and we concluded that the distributions of the $\sum$SFR for the RDAGN and the control galaxies are statistically similar. We found the same conclusions for the late-type RDAGN subsample and their control galaxies. Conversely, we found that the distribution of $\sum$SFR are statistically different for the early-type subsample of RDAGN and their controls (the null hypothesis can be rejected at the >5% level). The early-type RDAGN galaxies tend to have higher $\sum$SFR values (median value of -2.57 in logarithmic units of $M_\odot$ yr^{-1} kpc^{-2}) than the $\sum$SFR of their assigned control galaxies, which averages at -3.06 in logarithmic units of $M_\odot$ yr^{-1} kpc^{-2}.

For the distribution of total SFRs, which are shown in the bottom panels of Fig. 11, only the late-type subsample of RDAGN and their control galaxies exhibit a statistically similar distribution based on the A−D test ($p \sim 0.12$). While the distributions for the entire RDAGN, the early-type RDAGN subsample, and their assigned control galaxies most likely reveal physical differences, our analyses would benefit from more accurate SFR measurements, which would require decomposing each spectrum into SF, AGN, and shock components.

Our results are both consistent and at variance with the findings of do Nascimento et al. (2019), who use the MaNGA AGN and control sample selected by Rembold et al. (2017). By interpreting the p-values of A−D tests, both this study and do Nascimento et al. (2019) find that the $\sum$SFR are statistically similar for the AGN and controls. We report, however, a wider range of total SFRs; do Nascimento et al. (2019) find both the AGN and control sample to range in SFR from 10^{-3} to 10^1 $M_\odot$ yr^{-1}.

Neither our study nor that of do Nascimento et al. (2019) accounted for disk inclination when calculating $\sum$SFRs, which
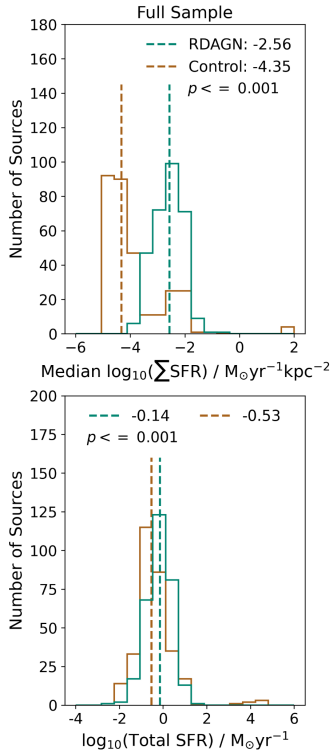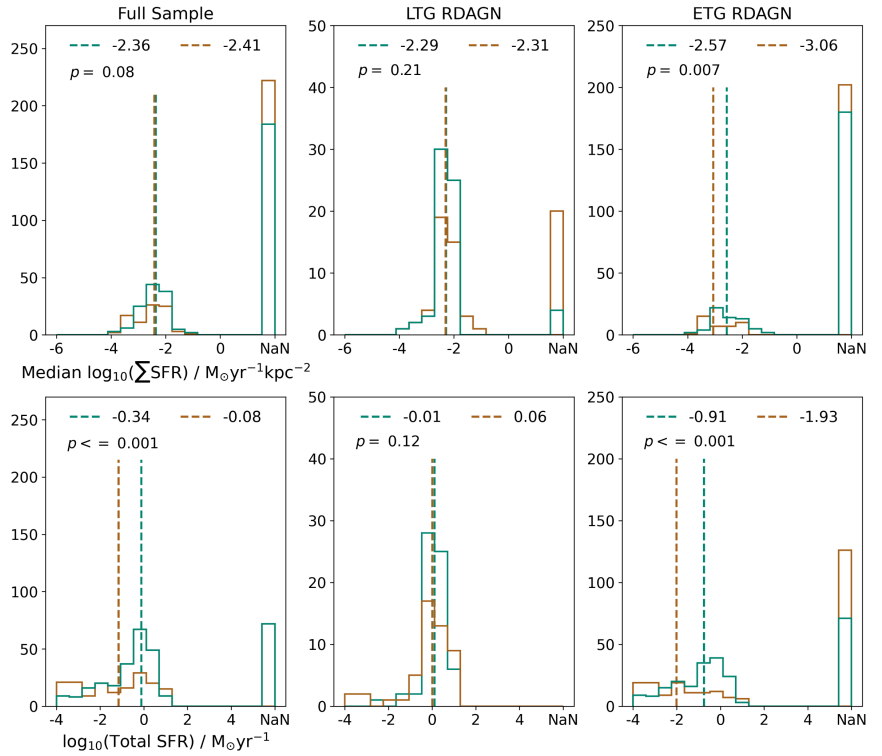

Fig. 11. *Left of the black vertical line*: distribution of the median ∑SFR (*top panel*) and for the total SFR (*bottom panel*) for RDAGN galaxies (green) and their controls (brown). We calculate these quantities using all spaxels with a $S/N > 0$ in all emission-lines used for classification. *Right of the black vertical line from left to right*: distribution of the median ∑SFR (*top panel*) and for the total SFR (*bottom panel*) for RDAGN galaxies (green) and their controls (brown) for the entire sample, LTGs, and ETGs. These quantities are derived from spaxels with a $S/N > 3$. When no spaxels in the galaxy meet the relevant criteria, the median or total SFR is set to "NaN".

could cause SFRs to be underestimated by a factor of ~0.2−0.4 dex due to not completely correcting dust attenuation (e.g., Morselli et al. 2016). However, given that the inclination of the RDAGN and of their assigned control sample were visually matched, our comparison does not suffer from a large inclination bias. Furthermore, both this study and do Nascimento et al. (2019) only consider HII and composite spaxels when calculating ∑SFR. The composite spaxels could be contaminated by shocks. Following Davies et al. (2017), future work could include calculating a more accurate SFR by decomposing the nuclear spectra into SF, AGN, and shock components.

6. Stellar age gradient

To find evidence for suppressed SF in RDAGN host galaxies and potentially in the control galaxies, we examined how the age of the stellar populations changes as a function of galactocentric distance. For this analysis, we use the gradient of the light-weighted log-age of the stellar population within a galactocentric distance of 0.5−2.0 R_e (hereafter α) from the Pipe3D VAC. When α is negative, the stellar populations become younger with distance from the center of the galaxy. Conversely, a positive age gradient indicates the stellar populations become older with increasing distance away from the galaxy's center. We compare α in stellar mass bins of 0.2 dex because previous studies have demonstrated that a correlation exists between a galaxy's M_* and stellar age gradient (e.g., González Delgado et al. 2014; Zheng et al. 2017; Goddard et al. 2017) and for comparison pur-

poses with the Pipe3D stellar, light-weighted age gradients binned in M_* for radio-quiet and radio-mode AGN host galaxies from Comerford et al. (2020). In Fig. 12, we present the Pipe3D stellar, light-weighted age gradient in M_* bins of 0.2 dex for the entire RDAGN and control samples as well as for RDAGN subsamples and their controls.

We find that the average stellar age gradients for the RDAGN sample and control sample as measured by Pipe3D are negative. We provide all the average values in the right-most column of Table 3. Their average values ($\alpha \sim -0.101$ for RDAGN and $\alpha \sim -0.097$ for the controls) are nearly identical indicating that the stellar populations within the RDAGN sample and the control sample become younger with distance from the center. These results may point to the inside-out suppression SF in these galaxies. Moreover, the consistency between the age gradient values between the AGN and controls indicates that there is no clear correlation between the current AGN activity and their host galaxies' SF history.

The average α value for late-type AGN host galaxies ($\alpha \sim -0.294$) is significantly steeper than early-type AGN host galaxies ($\alpha \sim -0.070$), which agrees with the results from previous MaNGA investigations (Goddard et al. 2017; Parikh et al. 2021). The negative radial stellar age gradients in LTGs are consistent with inside-out growth of the disk (González Delgado et al. 2015). On the other hand, strong AGN feedback can stop SF in the galaxy's center, and this inside-out quenching may also result in a negative age gradient (Comerford et al. 2020).
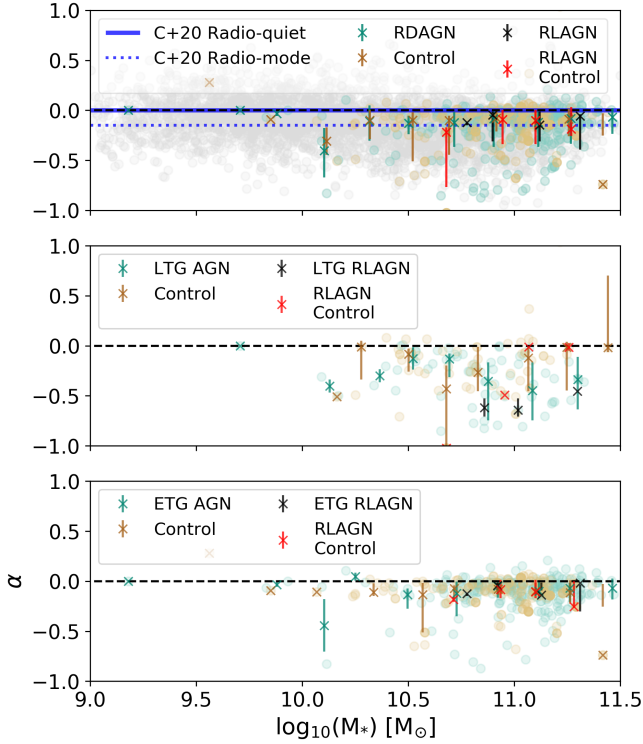
Fig. 12. Stellar, light-weighted age gradient (α) in M_* bins of 0.2 dex for RDAGN host galaxies (green), the full control sample (brown), RLAGN galaxies (black), RLAGN control galaxies (red), and the entire Pipe3D VAC (gray). A horizontal line is plotted at $\alpha = 0$ for reference. The x's represent the median value in each bin and the error bars represent the standard deviation of the sample. We provide the median α values for radio-quiet ($\alpha \sim 0$) and radio-mode ($\alpha \sim -0.15$) AGN from Comerford et al. (2020; C+20) in the solid and dotted blue lines, respectively.

The number of fibers in an IFU bundle affects the accuracy of the estimate of α (Ibarra-Medel et al. 2019). So, IFUs with a larger fiber bundle will have a more accurate measurement of α. Comerford et al. (2020) have investigated the magnitude of this effect on their sample of 406 MaNGA-AGN by looking at the stellar age gradients of galaxies that were observed with the largest MaNGA fiber bundle size (127 fibers, commensurate with a diameter of 32″5). Comerford et al. (2020) found that α decreased by ~0.05, but that did not change their result that radio-mode AGN host galaxies have more negative stellar age gradients when compared to radio-quiet AGN host galaxies. We find that the age gradients of RDAGN and control galaxies observed with the largest MaNGA fiber bundle decrease by ~0.10. These RDAGN and control galaxies have an identical average age gradient of $\alpha \sim -0.20 \pm 0.30$. By checking the magnitude of the effect of IFU fiber bundle size, we have reconfirmed the striking similarity between the RDAGN sample and control sample.

Residual AGN contamination can bias the stellar population fits (e.g., Cardoso et al. 2017). However, quantifying and rectifying this bias is beyond the scope of this work.

7. Discussion

In establishing whether or not AGN are responsible for quenching massive galaxies, we compare the SF properties of radio-detected AGN with non-active galaxies of similar stellar mass,

redshift, visual morphology, and inclination. AGN remain a key ingredient in cosmological models of galaxy evolution to reproduce the observed stellar mass and luminosity function and to prevent the formation of over-massive galaxies. However, the observational perspective has yielded mixed results, and therefore, the consensus on the effect of an AGN on their host galaxies' SFR has yet to be agreed upon. One of the most interesting results of our paper is that both radio-detected AGN and control galaxies typically lie below the main sequence, have broad SFR distributions, and exhibit negative stellar, light-weighted age gradients.

One possible explanation for the statistical similarity between the quenching patterns of our AGN-host galaxies and the control sample of non-active galaxies is the visibility timescales of AGN feedback. Much remains unclear about the timescales of the duty cycle of AGN, the duration of visible AGN episodes, the spatial scale at which these interactions occur and AGN variability (e.g., Alexander & Hickox 2012; Hickox et al. 2014; Sartori et al. 2018). Studies (e.g., Sánchez et al. 2018; Lacerda et al. 2020, and references therein) suggest that the timescales required to quench SF and the triggering of AGN activity could be completely different. Moreover, the fact that RLAGN appear to preferentially reside in ETGs, and that they are considerably more quenched than just RDAGN might suggest that radio activity is supported for a longer period, and quenching has occurred earlier in their host galaxies' lifetime. Additionally, how long it takes for AGN to have an observed effect on SF is still an unanswered question. Hence, the timescale of the suppression of SF from an AGN episode – or multiple AGN episodes – might be longer than the timescale of observable AGN activity (Harrison 2017). Furthermore, the flickering on and off of AGN may also play a role in maintaining galaxy quiescence, which could explain why we see little differences in the AGN and control galaxies.

An abundance of physical mechanisms have been evoked to explain galaxy quiescence. In our study, we do not expect that environmental effects play a significant role in quenching our RDAGN and control galaxies given their average stellar masses and redshifts ($\sim 10^{11} M_*$ and $z \sim 0$, respectively; Peng et al. 2010). Furthermore, results from SDSS-IV MaNGA-DR15 and the GASP survey suggest that for environmental quenching, quenching is expected to occur from the outside-in (e.g., Bluck et al. 2020a; Vulcani et al. 2020). Recent studies (e.g., Bluck et al. 2018, 2020a,b) have demonstrated that there is indeed a connection between quenching and the presence of central SMBH, which is consistent with expected models of quenching via AGN feedback. Our study reveals a similarity in the star-forming properties of radio-detected AGN host galaxies and non-active control galaxies, which may indicate that AGN feedback is likely not the only origin of inside-out quenching. Additionally, our results suggest that the effect of mass quenching from negative AGN feedback is indistinguishable from the effect of other mass quenching mechanisms such as virial shock heating in massive dark matter haloes, which prevents the accretion of cold gas onto galaxies (e.g., Birnboim & Dekel 2003; Kereš et al. 2005, 2009; Dekel & Birnboim 2006, 2008; Birnboim et al. 2007). Alternatively, SF may be quenched in galaxies without the expulsion and/or heating of gas. Instead, SF can be halted as a galaxy transitions to being dominated by a stellar spheroid, which stabilizes the gas disk and prevents it from fragmenting into star-forming clumps (i.e., morphological quenching; Martig et al. 2009).

Finding direct evidence for AGN feedback quenching SF in local radio galaxies would naturally be difficult because they

predominately reside in massive galaxies where SF has already been quenched. Additionally, the bulk of the energetic impact of a radio AGN is injected into the hot phase of their host galaxies' halo, where it only has a long-term effect on the SF history of the host galaxy.

Throughout this work, we compare our sample of RDAGN host galaxies to existing MaNGA AGN Catalogs (see Sect. 3.3). Several of these MaNGA AGN catalogs (Rembold et al. 2017; Wylezalek et al. 2018; Sánchez et al. 2018) select AGN with optical emission line ratios and cuts in the EW(Hα), and Comerford et al. (2020) take a multiwavelength approach. The main differences we see among these studies and our own is that the selection method determines the number of sources that are considered AGN host galaxies, and the intrinsic global properties they select for.

Our results are both consistent and in disagreement with those presented in do Nascimento et al. (2019), who compare the optically selected AGN sample from Rembold et al. (2017) with a control sample of non-active galaxies with similar global properties as each AGN host galaxy. Similar to our results, do Nascimento et al. (2019) find no differences in SFR between optically selected, late-type AGN host galaxies and their controls. However, do Nascimento et al. (2019) report that early-type AGN host galaxies typically exhibit higher SFRs and larger ionized gas masses than their assigned control galaxies. They attribute this result to AGN and SF activity being fueled by the same reservoir of gas. Hence, do Nascimento et al. (2019) suggest that it is unlikely that negative AGN feedback is occurring in the Rembold et al. (2017) MaNGA AGN sample. While our results do not indicate that AGN selected based on their current activity are responsible for suppressing their host galaxies' SF, they support the maintenance mode role that RDAGN are expected to play in the local Universe. We believe the difference in our findings for early-type AGN host galaxies is a result of sample selection methods.

We find that RDAGN, and classical RLAGN preferentially reside in ETGs, lie below the SFMS, and exhibit younger stellar populations with increasing distance from the host galaxies' centers. Our work compliments the findings presented in Comerford et al. (2020), who compare the SF properties of radio-mode and radio-quiet AGN host galaxies. They find that radio-quiet and radio-mode AGN preferentially reside in LTGs and ETGs, respectively, both populations fall below the SFMS, although radio-mode AGN host galaxies lie further below the SFMS, and that radio-mode AGN exhibit older stellar populations and have more negative stellar age gradients than the radio-quiet sample. From these results, Comerford et al. (2020) suggest that radio-mode AGN played a role in quenching SF in their host galaxies' pasts. Despite showing similar, albeit less obvious signs of past quenching, Comerford et al. (2020) do not provide a suggestion for the role radio-quiet AGN played in their host galaxies' past. Our study is different in that we compared these radio-selected AGN to non-active galaxies that match the stellar mass, redshift, visual morphology, and inclination of their RDAGN counterpart. Furthermore, our comparison to non-active galaxies, and our finding that there is no statistically significant difference between these two populations, is a more robust evaluation of the role RDAGN played in the SF quenching in the past.

Sánchez et al. (2018), and other IFS investigation of the role of AGN feedback in quenching SF (e.g., Lacerda et al. 2020, and references therein) have found that we cannot yet establish a causal connection between the presence of an AGN and the quenching of their host galaxies' SF. Instead, AGN activity and

SF processes present an apparent coevolution, which could be affected by the growth of galactic bulges. Similarly, the results presented here do not establish a casual connection between AGN activity and the halting of SF. Ours points to a scenario where there could be multiple quenching mechanisms occurring simultaneously, and where AGN play a role maintaining quiescence.

8. Conclusions

In this work, we have investigated whether negative AGN feedback is responsible for quenching massive galaxies. We combined the LoTSS DR2 and MaNGA DR16 data to form a sample of 1250 galaxies from which 307 RDAGN host galaxies were identified by combining selection techniques using global emission-line properties, radio luminosities, and WISE mid-infrared luminosities. Our investigation is the largest, IFS multi-wavelength study of AGN that has a control sample of non-active galaxies. Furthermore, thanks to the low frequencies and sensitivities reached by LOFAR, this study detects fainter radio emission from lower-powered jets – as well as remnant emission from sources that have recently shut-off their jet activity – than what was previously possible for radio surveys (e.g., NVSS, FIRST, etc.). Therefore, this work has resulted in significant progress toward understanding the effect of AGN feedback in a representative sample of low-luminosity AGN host galaxies.

We spatially mapped the dominant excitation mechanism of emission-line gas in RDAGN and control galaxies by combining the [NII] BPT, [SII] BPT, and the WHAN diagram. In regions ionized by toward, we calculated the SFR surface density ($\sum$SFR) using the dust corrected luminosity of Hα. We also used cumulative and gradient properties taken from the Pipe3D value added catalog to determine the relation of these galaxies to the SFMS and how the age of their stellar populations changes as a function of galactocentric radius. Our main results are summarized below:

1. RDAGN and control galaxies display a statistically similar distribution for the median toward rate surface density ($\sum$SFR). The fractional difference in $\sum$SFR of the RDAGN and its assigned control galaxy reveal that RDAGN host galaxies typically have higher SFRs.

2. RDAGN host galaxies lie below the SFMS, which suggests that RDAGN occupy galaxies with suppressed toward. RDAGN host galaxies have an average $\Delta \log_{10}(\text{SFR}) \sim -1.5$, while control galaxies fall further below the SFMS at an average $\Delta \log_{10}(\text{SFR}) \sim -2.3$.

3. The average SFR for RDAGN, as measured by Pipe3D, is higher ($\sim 10^{-1} M_\odot \text{ yr}^{-1}$) than the average SFR for the control sample of non-active galaxies ($\sim 10^{-1.8} M_\odot \text{ yr}^{-1}$). Taken together with the preceding points, we find no direct evidence that SF is quenched in RDAGN host galaxies. In fact, when compared to the control galaxies, our results may indicate that the effect of negative AGN feedback has not yet fully halted SF or that positive AGN feedback might be occurring in some late-type systems.

4. The average stellar, light-weighted age gradient for the RDAGN and control galaxies are identical at $\alpha \sim -0.10$. The negative age gradient implies that the stellar populations in the centers of galaxies are older than the populations on the outskirts. These results may point to inside-out quenching of SF in both samples. We find that early-type RDAGN host galaxies have a relatively flat average age gradient ($\alpha \sim -0.08$) whereas LTGs exhibit a steeper gradient ($\alpha \sim -0.26$).

This work demonstrates that the physical mechanisms behind the origin of the quenching of SF are yet to be fully understood. To further our understanding of how these RDAGN and their host galaxies are co-evolving, a detailed kinematic analysis could help determine the prevalence and velocity of outflows. Furthermore, the RDAGN sample in this work includes galaxies that have both AGN activity and some SF activity. Additional work is needed to decompose the radio emission into that coming from SF and that from jets. This will involve using LOFAR's international baselines to obtain high (subarcsecond) resolution images, which will allow us to identify genuine AGN emission and its effect on its host galaxy. We have already begun additional investigations on the molecular gas content of a subsample of these RDAGN host galaxies (Leslie et al., in prep.). We intend to use these observations to determine whether there is a deficiency of molecular gas in the central regions of RDAGN galaxies, which would quench central SF. Additionally, we could establish whether radio-mode AGN suppress SF either through their jet's mechanical energy heating the surrounding ISM and preventing molecular gas from radiatively cooling or if AGN-driven outflows expel the molecular gas out of the galaxy by correlating radio source size with stellar age and determining the SF efficiency.

References

Abazajian, K. N., Adelman-McCarthy, J. K., Agüeros, M. A., et al. 2009, ApJS, 182, 543
Ahumada, R., Prieto, C. A., Almeida, A., et al. 2020, ApJS, 249, 3
Aird, J., Coil, A. L., Georgakakis, A., et al. 2015, MNRAS, 451, 1892
Alexander, D. M., & Hickox, R. C. 2012, New Astron. Rev., 56, 93
Allen, M. G., Groves, B. A., Dopita, M. A., Sutherland, R. S., & Kewley, L. J. 2008, ApJS, 178, 20
Argudo-Fernández, M., Verley, S., Bergond, G., et al. 2015, A&A, 578, A110
Assef, R. J., Stern, D., Noirot, G., et al. 2018, ApJS, 234, 23
Baldwin, J. A., Phillips, M. M., & Terlevich, R. 1981, PASP, 93, 5
Becker, R. H., White, R. L., & Helfand, D. J. 1995, ApJ, 450, 559
Belfiore, F., Maiolino, R., Maraston, C., et al. 2016, MNRAS, 461, 3111
Best, P. N., & Heckman, T. M. 2012, MNRAS, 421, 1569
Best, P. N., Kauffmann, G., Heckman, T. M., et al. 2005a, MNRAS, 362, 25
Best, P. N., Kauffmann, G., Heckman, T. M., & Ivezić, Ž. 2005b, MNRAS, 362, 9
Binette, L., Magris, C. G., Stasińska, G., & Bruzual, A. G. 1994, A&A, 292, 13
Binney, J., & Tabor, G. 1995, MNRAS, 276, 663
Birnboim, Y., & Dekel, A. 2003, MNRAS, 345, 349
Birnboim, Y., Dekel, A., & Neistein, E. 2007, MNRAS, 380, 339
Bluck, A., Teimoorinia, H., Ellison, S. L., & Mendel, T. 2018, Am. Astron. Soc. Meet. Abstr., 231, 227.01
Bluck, A. F. L., Maiolino, R., Piotrowska, J. M., et al. 2020a, MNRAS, 499, 230
Bluck, A. F. L., Maiolino, R., Sánchez, S. F., et al. 2020b, MNRAS, 492, 96
Bower, R. G., Benson, A. J., Malbon, R., et al. 2006, MNRAS, 370, 645
Boyle, B. J., & Terlevich, R. J. 1998, MNRAS, 293, L49
Brinchmann, J., Charlot, S., White, S. D. M., et al. 2004, MNRAS, 351, 1151
Brinchmann, J., Kunth, D., & Durret, F. 2008, A&A, 485, 657
Bundy, K., Bershady, M. A., Law, D. R., et al. 2015, ApJ, 798, 7
Calistro Rivera, G., Williams, W. L., Hardcastle, M. J., et al. 2017, MNRAS, 469, 3468
Cano-Díaz, M., Ávila-Reese, V., Sánchez, S. F., et al. 2019, MNRAS, 488, 3929
Cardelli, J. A., Clayton, G. C., & Mathis, J. S. 1989, ApJ, 345, 245
Cardoso, L. S. M., Gomes, J. M., & Papaderos, P. 2017, A&A, 604, A99
Cattaneo, A., Faber, S. M., Binney, J., et al. 2009, Nature, 460, 213
Chen, C.-T. J., Hickox, R. C., Alberts, S., et al. 2013, ApJ, 773, 3
Cherinka, B., Andrews, B. H., Sánchez-Gallego, J., et al. 2019, AJ, 158, 74
Cid Fernandes, R., Stasińska, G., Schlickmann, M. S., et al. 2010, MNRAS, 403, 1036
Cid Fernandes, R., Stasińska, G., Mateus, A., & Vale Asari, N. 2011, MNRAS, 413, 1687
Ciotti, L., & Ostriker, J. P. 2001, ApJ, 551, 131
Ciotti, L., & Ostriker, J. P. 2007, ApJ, 665, 1038
Ciotti, L., Ostriker, J. P., & Proga, D. 2010, ApJ, 717, 708
Colless, M., Dalton, G., Maddox, S., et al. 2001, MNRAS, 328, 1039
Comerford, J. M., Negus, J., Müller-Sánchez, F., et al. 2020, ApJ, 901, 159
Condon, J. J., Cotton, W. D., Greisen, E. W., et al. 1998, AJ, 115, 1693
Condon, J. J., Cotton, W. D., & Broderick, J. J. 2002, AJ, 124, 675
Cresci, G., Marconi, A., Zibetti, S., et al. 2015, A&A, 582, A63
Crockett, R. M., Shabala, S. S., Kaviraj, S., et al. 2012, MNRAS, 421, 1603
Croft, S., van Breugel, W., de Vries, W., et al. 2006, ApJ, 647, 1040
Croton, D. J., Springel, V., White, S. D. M., et al. 2006, MNRAS, 365, 11
Daddi, E., Dickinson, M., Morrison, G., et al. 2007, ApJ, 670, 156
Davies, R. L., Groves, B., Kewley, L. J., et al. 2017, MNRAS, 470, 4974
Dekel, A., & Birnboim, Y. 2006, MNRAS, 368, 2
Dekel, A., & Birnboim, Y. 2008, MNRAS, 383, 119
Domínguez Sánchez, H., Huertas-Company, M., Bernardi, M., Tuccillo, D., & Fischer, J. L. 2018, MNRAS, 476, 3661
do Nascimento, J. C., Storchi-Bergmann, T., Mallmann, N. D., et al. 2019, MNRAS, 486, 5075
Drory, N., MacDonald, N., Bershady, M. A., et al. 2015, AJ, 149, 77
Elbaz, D., Daddi, E., Le Borgne, D., et al. 2007, A&A, 468, 33
Elbaz, D., Jahnke, K., Pantin, E., Le Borgne, D., & Letawe, G. 2009, A&A, 507, 1359

Ellison, S. L., Teimoorinia, H., Rosario, D. J., & Mendel, J. T. 2016, MNRAS, 458, L34

Espinosa-Ponce, C., Sánchez, S. F., Morisset, C., et al. 2020, MNRAS, 494, 1622

Fabian, A. C. 2012, ARA&A, 50, 455

Feain, I. J., Papadopoulos, P. P., Ekers, R. D., & Middelberg, E. 2007, ApJ, 662, 872

Gilli, R., Mignoli, M., Peca, A., et al. 2019, A&A, 632, A26

Goddard, D., Thomas, D., Maraston, C., et al. 2017, MNRAS, 466, 4731

Gomes, J. M., Papaderos, P., Kehrig, C., et al. 2016, A&A, 588, A68

González Delgado, R. M., Pérez, E., Cid Fernandes, R., et al. 2014, A&A, 562, A47

González Delgado, R. M., García-Benito, R., Pérez, E., et al. 2015, A&A, 581, A103

Gunn, J. E., Siegmund, W. A., Mannery, E. J., et al. 2006, AJ, 131, 2332

Gürkan, G., Hardcastle, M. J., Jarvis, M. J., et al. 2015, MNRAS, 452, 3776

Gürkan, G., Hardcastle, M. J., Smith, D. J. B., et al. 2018, MNRAS, 475, 3010

Haehnelt, M. G., & Kauffmann, G. 2000, MNRAS, 318, L35

Hales, C. A. 2013, ArXiv e-prints [arXiv:1312.4602]

Hardcastle, M. J., Ching, J. H. Y., Virdee, J. S., et al. 2013, MNRAS, 429, 2407

Hardcastle, M. J., Gürkan, G., van Weeren, R. J., et al. 2016, MNRAS, 462, 1910

Hardcastle, M. J., Williams, W. L., Best, P. N., et al. 2019, A&A, 622, A12

Häring, N., & Rix, H.-W. 2004, ApJ, 604, L89

Harrison, C. M. 2017, Nat. Astron., 1, 0165

Heckman, T. M. 1980, A&A, 87, 152

Heckman, T. M., & Best, P. N. 2014, ARA&A, 52, 589

Herpich, F., Mateus, A., Stasińska, G., Cid Fernandes, R., & Vale Asari, N. 2016, MNRAS, 462, 1826

Hickox, R. C., Mullaney, J. R., Alexander, D. M., et al. 2014, ApJ, 782, 9

Ibarra-Medel, H. J., Avila-Reese, V., Sánchez, S. F., González-Samaniego, A., & Rodríguez-Puebla, A. 2019, MNRAS, 483, 4525

Ichikawa, K., Ueda, J., Bae, H.-J., et al. 2019, ApJ, 870, 65

Intema, H. T., Jagannathan, P., Mooley, K. P., & Frail, D. A. 2017, A&A, 598, A78

Ishibashi, W., & Fabian, A. C. 2012, MNRAS, 427, 2998

Jackson, T. M., Rosario, D. J., Alexander, D. M., et al. 2020, MNRAS, 498, 2323

Kauffmann, G., Heckman, T. M., Tremonti, C., et al. 2003, MNRAS, 346, 1055

Keel, W. C., Lintott, C. J., Maksym, W. P., et al. 2017, ApJ, 835, 256

Kennicutt, R. C., Jr. 1998, ARA&A, 36, 189

Kereš, D., Katz, N., Weinberg, D. H., & Davé, R. 2005, MNRAS, 363, 2

Kereš, D., Katz, N., Davé, R., Fardal, M., & Weinberg, D. H. 2009, MNRAS, 396, 2332

Kewley, L. J., Dopita, M. A., Sutherland, R. S., Heisler, C. A., & Trevena, J. 2001, ApJ, 556, 121

Kewley, L. J., Groves, B., Kauffmann, G., & Heckman, T. 2006, MNRAS, 372, 961

Kewley, L. J., Dopita, M. A., Leitherer, C., et al. 2013, ApJ, 774, 100

Klamer, I. J., Ekers, R. D., Sadler, E. M., & Hunstead, R. W. 2004, ApJ, 612, L97

Lacerda, E. A. D., Cid Fernandes, R., Couto, G. S., et al. 2018, MNRAS, 474, 3727

Lacerda, E. A. D., Sánchez, S. F., Cid Fernandes, R., et al. 2020, MNRAS, 492, 3073

Lang, D. 2014, AJ, 147, 108

Lang, D., Hogg, D. W., & Schlegel, D. J. 2016, AJ, 151, 36

Law, D. R., Cherinka, B., Yan, R., et al. 2016, AJ, 152, 83

Leslie, S. K., Kewley, L. J., Sanders, D. B., & Lee, N. 2016, MNRAS, 455, L82

López-Cobá, C., Sánchez, S. F., Bland-Hawthorn, J., et al. 2019, MNRAS, 482, 4032

López-Cobá, C., Sánchez, S. F., Anderson, J. P., et al. 2020, AJ, 159, 167

Magliocchetti, M., Lutz, D., Santini, P., et al. 2016, MNRAS, 456, 431

Magliocchetti, M., Popesso, P., Brusa, M., & Salvato, M. 2018, MNRAS, 473, 2493

Martig, M., Bournaud, F., Teyssier, R., & Dekel, A. 2009, ApJ, 707, 250

McNamara, B. R., & Nulsen, P. E. J. 2007, ARA&A, 45, 117

Morselli, L., Renzini, A., Popesso, P., & Erfanianfar, G. 2016, MNRAS, 462, 2355

Mullaney, J. R., Daddi, E., Béthermin, M., et al. 2012, ApJ, 753, L30

Mullaney, J. R., Alexander, D. M., Aird, J., et al. 2015, MNRAS, 453, L83

Nesvadba, N. P. H., Lehnert, M. D., De Breuck, C., Gilbert, A. M., & van Breugel, W. 2008, A&A, 491, 407

Nesvadba, N. P. H., Boulanger, F., Salomé, P., et al. 2010, A&A, 521, A65

Nesvadba, N. P. H., Bicknell, G. V., Mukherjee, D., & Wagner, A. Y. 2020, A&A, 639, L13

Netzer, H. 2009, MNRAS, 399, 1907

Noeske, K. G., Faber, S. M., Weiner, B. J., et al. 2007, ApJ, 660, L47

Oh, K., Yi, S. K., Schawinski, K., et al. 2015, ApJS, 219, 1

Osterbrock, D. E., & Ferland, G. J. 2006, Astrophysics of Gaseous Nebulae and Active Galactic Nuclei (Sausalito: University Science Books)

Papaderos, P., Gomes, J. M., Vílchez, J. M., et al. 2013, A&A, 555, L1

Parikh, T., Thomas, D., Maraston, C., et al. 2021, MNRAS, 502, 5508

Peng, Y.-J., Lilly, S. J., Kovač, K., et al. 2010, ApJ, 721, 193

Pillepich, A., Nelson, D., Springel, V., et al. 2019, MNRAS, 490, 3196

Pitchford, L. K., Hatziminaoglou, E., Feltre, A., et al. 2016, MNRAS, 462, 4067

Rembold, S. B., Shimoia, J. S., Storchi-Bergmann, T., et al. 2017, MNRAS, 472, 4382

Rich, J. A., Kewley, L. J., & Dopita, M. A. 2011, ApJ, 734, 87

Rodríguez Zaurín, J., Holt, J., Tadhunter, C. N., & González Delgado, R. M. 2007, MNRAS, 375, 1133

Rosario, D. J., Santini, P., Lutz, D., et al. 2012, A&A, 545, A45

Roy, N., Bundy, K., Cheung, E., et al. 2018, ApJ, 869, 117

Sabater, J., Best, P. N., Hardcastle, M. J., et al. 2019, A&A, 622, A17

Sadler, E. M., Jackson, C. A., Cannon, R. D., et al. 2002, MNRAS, 329, 227

Salpeter, E. E. 1955, ApJ, 121, 161

Sánchez, S. F. 2020, ARA&A, 58, 99

Sánchez, S. F., Pérez, E., Sánchez-Blázquez, P., et al. 2016a, Rev. Mex. Astron. Astrofis., 52, 21

Sánchez, S. F., Pérez, E., Sánchez-Blázquez, P., et al. 2016b, Rev. Mex. Astron. Astrofis., 52, 171

Sánchez, S. F., Avila-Reese, V., Hernandez-Toledo, H., et al. 2018, Rev. Mex. Astron. Astrofis., 54, 217

Sartori, L. F., Schawinski, K., Trakhtenbrot, B., et al. 2018, MNRAS, 476, L34

Sarzi, M., Shields, J. C., Schawinski, K., et al. 2010, MNRAS, 402, 2187

Savage, B. D., & Mathis, J. S. 1979, ARA&A, 17, 73

Schaye, J., Crain, R. A., Bower, R. G., et al. 2015, MNRAS, 446, 521

Schirmer, M., Malhotra, S., Levenson, N. A., et al. 2016, MNRAS, 463, 1554

Shimizu, T. T., Mushotzky, R. F., Meléndez, M., Koss, M., & Rosario, D. J. 2015, MNRAS, 452, 1841

Shimwell, T. W., Röttgering, H. J. A., Best, P. N., et al. 2017, A&A, 598, A104

Shimwell, T. W., Tasse, C., Hardcastle, M. J., et al. 2019, A&A, 622, A1

Shimwell, T. W., Hardcastle, M. J., Tasse, C., et al. 2022, A&A, 659, A1

Shin, J., Woo, J.-H., Chung, A., et al. 2019, ApJ, 881, 147

Silverman, J. D., Kovač, K., Knobel, C., et al. 2009, ApJ, 695, 171

Singh, R., van de Ven, G., Jahnke, K., et al. 2013, A&A, 558, A43

Smee, S. A., Gunn, J. E., Uomoto, A., et al. 2013, AJ, 146, 32

Smolčić, V., Novak, M., Bondi, M., et al. 2017, A&A, 602, A1

Speagle, J. S., Steinhardt, C. L., Capak, P. L., & Silverman, J. D. 2014, ApJS, 214, 15

Stanley, F., Harrison, C. M., Alexander, D. M., et al. 2015, MNRAS, 453, 591

Stasińska, G., Cid Fernandes, R., Mateus, A., Sodré, L., & Asari, N. V. 2006, MNRAS, 371, 972

Stasińska, G., Vale Asari, N., Cid Fernandes, R., et al. 2008, MNRAS, 391, L29

Stern, J., & Laor, A. 2013, MNRAS, 431, 836

Stoughton, C., Lupton, R. H., Bernardi, M., et al. 2002, AJ, 123, 485

Thomas, D., Steele, O., Maraston, C., et al. 2013, MNRAS, 431, 1383

van Haarlem, M. P., Wise, M. W., Gunst, A. W., et al. 2013, A&A, 556, A2

Venturi, G., Cresci, G., Marconi, A., et al. 2021, A&A, 648, A17

Vulcani, B., Fritz, J., Poggianti, B. M., et al. 2020, ApJ, 892, 146

Wright, E. L., Eisenhardt, P. R. M., Mainzer, A. K., et al. 2010, AJ, 140, 1868

Wylezalek, D., Zakamska, N. L., Greene, J. E., et al. 2018, MNRAS, 474, 1499

Wylezalek, D., Flores, A. M., Zakamska, N. L., Greene, J. E., & Riffel, R. A. 2020, MNRAS, 492, 4680

Yan, R., & Blanton, M. R. 2012, ApJ, 747, 61

Yan, R., Tremonti, C., Bershady, M. A., et al. 2016a, AJ, 151, 8

Yan, R., Bundy, K., Law, D. R., et al. 2016b, AJ, 152, 197

York, D. G., Adelman, J., Anderson, J. E., Jr., et al. 2000, AJ, 120, 1579

Young, J. E., Eracleous, M., Shemmer, O., et al. 2014, MNRAS, 438, 217

Yuan, F., & Narayan, R. 2014, ARA&A, 52, 529

Zhang, K., Wang, T., Dong, X., & Lu, H. 2008, ApJ, 685, L109

Zheng, Z., Wang, H., Ge, J., et al. 2017, MNRAS, 465, 4572

Appendix A: Extra Tables

Table A.1. MaNGA plateifu for RDAGN host galaxies and their assigned control galaxy.

RLAGN plateifu	Control plateifu	RLAGN plateifu	Control plateifu	RLAGN plateifu	Control plateifu	RLAGN plateifu	Control plateifu
9891-3704	9507-6103	9026-12705	8439-12702	8716-3702	8721-6102	8447-1902	8440-3702
9891-3702	8713-3702	9025-9101	9045-12705	8712-12705	8978-12704	8447-12704	8315-12702
9883-9101	9044-12703	9025-12704	8984-12705	8712-12704	8602-12705	8446-3701	8718-3702
9883-6101	8326-3702	9025-12701	9501-12703	8711-12704	8243-12703	8445-12702	8262-6103
9883-3702	8440-3702	9024-3703	8713-3702	8613-6102	8943-3701	8439-3704	8568-9102
9881-9101	8149-12704	9024-12702	9085-6104	8613-3702	8944-3702	8341-12702	8451-6102
9881-3701	8588-3701	9002-9101	9038-12703	8606-9101	8555-6101	8335-9101	8315-12702
9871-12702	8602-12705	9002-3703	8989-6104	8604-6102	8997-6101	8335-6103	8315-12702
9870-1901	8547-1902	9002-12703	8613-12704	8604-12703	8947-12704	8333-9102	8141-6104
9868-6104	9041-3701	9002-12702	8315-12702	8602-12701	8602-12705	8333-6103	8326-9101
9868-3704	8485-3703	9000-9102	8613-12704	8601-12704	8464-9101	8333-6101	8326-3702
9865-9101	9487-12705	9000-12703	8139-9102	8600-12703	8936-12702	8333-3703	9185-3703
9864-6104	8258-3703	9000-12701	8548-3701	8597-9101	8452-6103	8333-12704	8948-6104
9864-3702	8313-3702	8999-3702	9891-3701	8597-3704	8566-6104	8333-12701	8715-12703
9864-12705	8332-6101	8997-9101	8139-9102	8597-3703	9182-6103	8332-6104	8455-6104
9864-12702	8452-6103	8997-6104	8612-6101	8597-3701	9486-1902	8332-12705	8312-9101
9864-12701	8939-6103	8997-6103	8465-3703	8597-12702	9505-12701	8331-9101	8315-12702
9510-6104	9507-6103	8997-6102	8989-6104	8595-6101	9041-3701	8331-3702	8258-3703
9510-12705	8131-6103	8997-1902	9501-3702	8595-12704	9184-9101	8331-3701	9182-1901
9508-9102	8996-3702	8995-3703	8715-3703	8592-12703	8330-12705	8331-12701	9026-12704
9508-12702	9026-6104	8995-12705	8443-12703	8591-6101	8252-3702	8330-6103	9509-6102
9507-3701	8980-6102	8995-12703	8315-12702	8591-3701	8938-6101	8325-6101	8445-6102
9485-6103	9028-6104	8993-12705	8249-12703	8588-6104	8465-3703	8323-6101	8947-12704
9485-6102	9041-3701	8992-9102	8149-12704	8588-6102	8313-3702	8323-1902	9029-6101
9485-6101	8443-12703	8991-9102	8943-3701	8568-1901	9485-1902	8322-3702	9486-6101
9183-12704	8979-9101	8991-3702	8713-3702	8566-6101	8141-6104	8319-9102	7958-6104
9182-3704	8313-3702	8990-12702	8604-12701	8555-6103	8483-6104	8319-6104	9486-6104
9181-6103	8713-3702	8989-6103	8462-6102	8555-3704	8555-3702	8319-6103	9883-6103
9181-3704	8948-6104	8989-12704	9045-12705	8555-12704	8485-3701	8317-6103	8948-6104
9181-3702	8588-3701	8985-3703	8612-3704	8555-12701	9044-12703	8317-12701	8315-12702
9181-12704	9486-6101	8984-3704	8253-3702	8554-6104	9505-12701	8315-6103	8713-3702
9181-12703	9509-12705	8983-1902	8313-3704	8554-6103	9041-3701	8313-12705	8258-12704
9181-12702	8547-12703	8983-12703	9881-6103	8554-6102	8948-6104	8309-12702	8483-6104
9045-6103	9185-3703	8982-3701	8999-6103	8554-3702	8713-3702	8263-3702	8548-3701
9045-6102	8131-6103	8980-12703	8244-6102	8553-6102	9487-12705	8262-9101	9034-12704
9045-3704	8997-12704	8979-12701	8443-12703	8553-3703	9184-6102	8261-6101	8713-3702
9045-3701	8713-3702	8978-9101	9881-12705	8553-12704	9034-1901	8261-3703	9182-1901
9045-1902	8313-3702	8977-9101	8262-6103	8552-9102	8713-6103	8261-3702	8713-3702
9045-12701	8943-3701	8977-3703	8713-3702	8552-9101	9038-12703	8259-3703	8718-6103
9044-6104	9883-6104	8952-6102	8140-3702	8552-6103	8141-6104	8258-6102	9182-6103
9044-3704	8258-3703	8952-3703	9881-3702	8551-3704	8440-3702	8257-3701	8600-6104
9044-3703	8313-3704	8952-12702	9025-6103	8550-3704	8259-3702	8255-6104	8274-6103
9044-3702	8455-6103	8952-12701	8600-3704	8550-12702	8978-12704	8255-6101	8567-6104
9044-12705	8721-6102	8950-12705	8603-6102	8549-9101	8309-9101	8253-1901	8249-1902
9044-12704	8332-6101	8948-6103	8980-3701	8549-12702	8602-12705	8249-6103	8938-6101
9044-12702	8713-3702	8948-1902	9486-1902	8547-9101	8984-9101	8247-9102	8483-6104
9044-12701	8313-6102	8947-6104	8938-6101	8486-3704	9870-3704	8247-6101	8551-1901
9043-6103	9041-3701	8947-6101	8713-3702	8486-3701	8713-6103	8244-9102	9891-3701
9043-3702	9486-1902	8947-3704	8326-9101	8485-9101	8326-3702	8244-6103	8483-6104
9043-12703	8980-12702	8946-9102	8936-12702	8485-12703	8566-6104	8244-3704	9041-3701
9043-12702	8261-3704	8946-6104	8948-6104	8483-6102	8313-3702	8244-3701	8993-3703
9042-3701	8713-3702	8946-3703	8978-1901	8482-3703	8999-6103	8243-9102	8313-3702

Table A.1. continued.

RLAGN plateifu	Control plateifu	RLAGN plateifu	Control plateifu	RLAGN plateifu	Control plateifu	RLAGN plateifu	Control plateifu
9041-6103	8948-6104	8946-1902	8313-3702	8482-1901	9485-1902	8150-6104	9028-12702
9041-3704	8938-6104	8946-12703	8455-6103	8482-12702	9026-12704	8150-1901	9486-1902
9039-6103	8713-3702	8946-12701	9487-12705	8481-9101	8481-6101	8149-12705	9487-12705
9039-6101	8943-3701	8943-9101	9182-6101	8481-3704	8455-6103	8146-12705	9487-9101
9039-1902	8613-3703	8943-3704	9041-3701	8466-3701	8718-3702	8146-12704	9184-9101
9039-12701	9184-9101	8943-3703	8980-6102	8465-6101	8483-6104	8143-6104	9182-6103
9038-12702	9034-12704	8943-3702	8140-3702	8465-12704	9872-12705	8143-6103	9038-6101
9037-6104	8984-9101	8942-12702	8602-12705	8464-1902	7960-1902	8135-9101	8315-12702
9037-6103	9487-1901	8942-12701	8313-3701	8462-3702	9041-3701	8135-6103	9487-12705
9037-12704	8715-6104	8941-1901	8459-3703	8461-9101	8326-9101	8135-3703	8612-3704
9036-3703	8139-9102	8938-9102	10001-9102	8461-3703	8713-3702	8135-12701	8459-3703
9035-6103	9865-6102	8938-3704	9045-12705	8461-12701	8717-9102	8131-6102	8313-3702
9035-3704	8980-3702	8937-1902	8987-1902	8459-6104	8551-6102	8131-12705	8330-12705
9034-6104	9045-12705	8932-1902	8440-3701	8459-3701	8938-1901	8131-12702	8135-6102
9033-9101	8274-6103	8725-6103	9182-6103	8456-6103	8939-6103	7992-12701	8309-9101
9033-6104	8943-3701	8724-6101	8482-6103	8456-3702	9507-6101	7960-9102	9045-12705
9033-6103	8326-9101	8724-12703	8249-6104	8456-3701	8253-3702	7960-1901	8547-1902
9031-12703	8996-9102	8721-9102	8713-3702	8454-9102	8588-12701	7958-9102	8939-6103
9029-9102	9038-6101	8721-6103	8984-12705	8454-6103	8274-6103	7958-3701	9002-6102
9029-9101	8612-6101	8721-12703	8483-6104	8452-6102	9038-3704	7957-6103	8485-3703
9029-12703	8936-12702	8721-12701	8312-9101	8452-3703	8948-6104	7957-12703	9042-6104
9028-9102	8936-12705	8720-12702	8330-12705	8452-3702	8313-3702	7443-9102	9000-3703
9028-3701	8315-12702	8717-6103	9002-6102	8447-6104	8948-9102	7443-6104	8548-3701
9027-3704	8258-3703	8717-3702	8274-6103	8447-6102	8948-6104	10001-6104	8452-6103
9026-6103	8484-6101	8717-1902	8555-3702	8447-3702	8713-3702		

Table A.2. MaNGA galaxies excluded from the final RDAGN sample.

AGN ID	RA [deg]	Dec [deg]	Justification for Excluding from Final Sample
9031-9102	241.3982	44.20613	Cube Quality: CRITICAL
9183-3701	119.968	38.24004	Cube Quality: CRITICAL
8613-12705	255.6771	34.05999	Cube Quality: CRITICAL
9182-9101	120.1768	40.0273	Cube Quality: CRITICAL
8995-12704	175.5114	55.39062	Cube Quality: CRITICAL
8995-3704	175.602	54.77419	Cube Quality: CRITICAL
8995-12701	174.3928	54.85328	Cube Quality: CRITICAL
8995-6104	176.508	55.41962	Cube Quality: CRITICAL
8952-9102	205.6328	26.48724	Cube Quality: CRITICAL
9024-6101	221.6665	33.30122	Cube Quality: CRITICAL
8253-9101	157.6605	44.01272	Cube Quality: BAD OMEGA
9486-9101	120.7992	39.88577	Cube Quality: BAD OMEGA
8147-12705	117.9821	27.30297	Cube Quality: BAD OMEGA
9035-9101	235.447	45.556	Cube Quality: BAD OMEGA
8940-12704	122.0924	26.27565	Cube Quality: BAD OMEGA
9181-12701	118.5709	38.22089	Cube Quality: BAD OMEGA
8549-3703	241.4164	46.84656	Cube Quality: BAD OMEGA
8329-12705	214.5477	44.47428	Cube Quality: BAD OMEGA
8447-6103	206.173	40.4673	Cube Quality: BAD OMEGA
9031-9101	239.1646	45.54078	Cube Quality: BAD OMEGA
8439-12705	143.2881	49.05032	Cube Quality: BAD OMEGA
8247-6103	136.72	41.40825	Cube Quality: BAD OMEGA
8952-12704	205.2358	26.48672	Cube Quality: BAD OMEGA
8568-12704	155.543	38.51782	Cube Quality: BAD OMEGA
8612-12702	253.9464	39.31054	Cube Quality: BAD OMEGA
8945-1902	174.4782	47.46635	Cube Quality: BAD FLUX
8945-3704	175.1973	46.54049	Cube Quality: BAD FLUX
8945-6102	173.7012	46.98995	Cube Quality: BAD FLUX
8482-9101	241.7996	48.57256	No radio emission at > 3xrms
8603-6104	247.42	40.68695	No radio emission at > 3xrms
8552-6104	229.0521	45.23306	No radio emission at > 3xrms
8554-12701	182.2852	35.63581	No radio emission at > 3xrms
9029-12704	247.217	42.81201	No radio emission at > 3xrms
8326-3703	215.2749	48.30817	No radio emission at > 3xrms
8330-3702	203.8965	40.11109	No radio emission at > 3xrms
8257-1902	166.2978	46.10294	No radio emission at > 3xrms
8612-1902	254.0966	38.36347	No radio emission at > 3xrms
8459-12701	147.379	42.13029	No radio emission at > 3xrms
8712-1901	119.9737	55.37482	No radio emission at > 3xrms
8554-12703	182.7931	37.51535	No radio emission at > 3xrms
8326-6104	216.2561	47.95349	No radio emission at > 3xrms
8254-6103	162.9892	44.76013	No radio emission at > 3xrms
8595-3701	218.8973	50.18998	No radio emission at > 3xrms
9002-3701	222.8336	30.66383	No radio emission at > 3xrms
9028-3703	243.7375	30.75408	No radio emission at > 3xrms
8548-3703	243.044	47.90643	No radio emission at > 3xrms
8712-3704	122.2451	53.50988	No radio emission at > 3xrms

Table A.2. continued.

AGN ID	RA [deg]	Dec [deg]	Justification for Excluding from Final Sample
9865-12703	223.1398	50.92284	No radio emission at > 3xrms
9024-3702	221.792	33.21047	No radio emission at > 3xrms
8329-1901	214.4221	45.46582	No radio emission at > 3xrms
8253-6104	158.2514	42.92842	No radio emission at > 3xrms
8549-3704	243.1854	45.35201	No radio emission at > 3xrms
8721-12704	135.2365	54.95451	No radio emission at > 3xrms
8948-12702	164.9711	50.0152	No radio emission at > 3xrms
8993-3704	166.0866	46.0561	No radio emission at > 3xrms
8253-6102	158.533	42.80921	No radio emission at > 3xrms
8481-1902	237.6539	53.39062	No radio emission at > 3xrms
9869-9101	246.5913	40.91184	No radio emission at > 3xrms
9026-3704	251.3779	43.58164	No radio emission at > 3xrms
9883-12703	256.5416	33.60413	No radio emission at > 3xrms
8444-9101	200.6449	33.15709	No radio emission at > 3xrms
8253-6103	156.9885	43.31827	No radio emission at > 3xrms
7957-6102	258.2711	35.26862	No radio emission at > 3xrms
8252-12702	145.5308	48.15487	No radio emission at > 3xrms
8592-9102	224.4149	53.00634	No radio emission at > 3xrms
8601-3702	247.6121	40.72508	No radio emission at > 3xrms
8712-6104	121.5857	55.46234	No radio emission at > 3xrms
8716-3703	123.5062	52.75246	No radio emission at > 3xrms
8948-1901	165.7391	50.67024	No radio emission at > 3xrms
8480-9101	194.3831	28.47694	No maps available from MaNGA
8479-12701	195.0339	27.977	No maps available from MaNGA
8454-1902	154.7634	44.03303	No control candidates with z or M_* that varies < 30%